



PONTIFICIA UNIVERSIDAD CATÓLICA DE CHILE
FACULTAD DE FÍSICA
INSTITUTO DE ASTROFÍSICA

The Exceptional X-ray Evolution of SN 1996cr in High Resolution

BY

JONATHAN ALEXANDER QUIROLA VÁSQUEZ

Tesis presentada a la Facultad de Física de la Pontificia Universidad Católica de Chile,
para optar al grado académico de Magíster en Astrofísica.

SUPERVISOR : Dr. Franz Bauer

CORRECTORS : Dr. Stephane Blondin

Dr. Jose Luis Prieto

October 5th, 2018

Santiago, Chile

©2018, Jonathan Quirola

Declaration

The work described in this thesis was undertaken between 2016 and 2018 while the author was a researcher master student under the supervision of Professor Franz Bauer, in the Institute of Astrophysics at the Pontificia Universidad Católica de Chile. This work has not been submitted for any other degree at the Pontificia Universidad Católica de Chile or any other university.

©2018, Jonathan Quirola

Se autoriza la reproducción total o parcial, con fines académicos, por cualquier medio o procedimiento, incluyendo la cita bibliográfica del documento.

Para Arita, mis padres y mi hermanito

Acknowledgements

I am deeply grateful to Prof. Franz Bauer for being an excellent advisor, by his infinite patience (especially during my first year), and for teaching me so much during these years where I have grown a lot as a naive, novice astronomer and a person with his support. Thanks to V. V. Dwarkadas, C. Badenes, W. N. Brandt, T. Nymark, D. Walton, D. Dewey, and N. Vásquez for their important suggestions to finish this thesis. Thanks to my parents, Margoth and Gonzalo, for their unconditional love and support through my career from childhood to now. Also, I am thankful to my brother, Erick, for being an important support and his friendship. My sincere gratitude to Aracely, thank you for your trust, support and love, for making me happy every day and for inspiring me to reach our dreams. Thanks to the people who we have shared a great time in Pontificia Universidad Católica de Chile. Special thanks to my mates and friends Rodrigo, Ismael, Camila(s), Rafael, Katy, always keeping a great working atmosphere. Thanks to my gabrielinos (Andres, Cucus, Maelo, Pazmi, Pistola) and poli (Nico, Daco, Jefe, Gaby, Andre, Darwin, Jimmy) friends, I have never forgotten you guys.

Contents

1	Introduction	11
1.1	General features of SNe type II _n	11
1.2	SN1996cr	13
2	Data analysis	19
2.1	Chandra X-ray Observatory	19
2.2	<i>XMM-Newton</i>	23
3	Methodology and Model	26
3.1	Epoch 2009	28
3.1.1	Single plasma component (M1)	28
3.1.2	Line Geometry	32
3.1.3	Single Plasma Component with Shellblur (M2)	40
3.1.4	Multiple Plasma Components with Shellblur (M3–M6)	40
3.2	2000, 2001, 2004, 2013, 2014, 2016 and 2018 epochs	45
4	Results and discussion	52
4.1	Interpretation of Model M5 at 2009 epoch	52
4.2	Time Evolution of Parameters	57
5	Conclusions and future work	73

Bibliography	87
A XMM-Newton Spectra	88

List of Tables

2.1	X-ray observations used in this work.	25
3.1	Statistic values associated with each model for the 2000, 2004 and 2009 epochs.	46
3.2	Spectral parameters for model M5 at different epochs.	51
4.1	Best-fit abundance distributions as deduced from model M5.	68

List of Figures

1.1	SNe canonical scenario cartoon.	14
1.2	X-ray light curves sample of type IIIn SNe.	18
2.1	HETG pattern observation example.	21
2.2	SN 1196cr detected by <i>XMM-Newton</i> (<i>pn</i>).	22
3.1	<i>Chandra</i> grating data and M1 best-fit model for 2009 epoch.	29
3.2	H-like Si and Fe in velocity space.	31
3.3	Examples of different expanding shock structure geometries.	34
3.4	Illustration of the “shellblur” model showing the parameters configuration.	35
3.5	Comparison of velocity profiles as a function of inclination angle.	36
3.6	Close-up of H-like and He-like lines considering two scenarios.	37
3.7	Error confidence maps of parameters θ_{\min} and i	38
3.8	Close-up spectra of several H-like and He-like considering model M2.	39
3.9	<i>Chandra</i> grating data and the best-fit model M5 for 2009 epoch.	43
3.10	Best-fit model M5 and its components.	44
3.11	<i>Chandra</i> grating data and the best-fit model M5 for 2000 epoch.	47
3.12	<i>Chandra</i> grating data and best-fit model M5 for 2004 epoch.	48
3.13	Fe emission of 2000 epoch considering the bullet additional component.	50
4.1	Evolution of the foreground absorption and NEI temperatures.	59
4.2	Evolution of the geometrical model velocity expansion and opening angle.	63

4.3	Evolution of the geometrical model absorption from inner ejecta and flux.	66
4.4	Evolution of the Fe and Si abundances.	68
4.5	Relative abundances derived from components C1 and C2.	69
A.1	<i>XMM-Newton pn</i> -camera data and the best-fit model M5 for epoch 2001. .	89
A.2	<i>XMM-Newton pn</i> -camera data and the best-fit model M5 for epoch 2013. .	89
A.3	<i>XMM-Newton pn</i> -camera data and the best-fit model M5 for epoch 2014. .	90
A.4	<i>XMM-Newton pn</i> -camera data and the best-fit model M5 for epoch 2016. .	90
A.5	<i>XMM-Newton pn</i> -camera data and the best-fit model M5 for epoch 2018. .	90

Resumen

En esta tesis presentamos un análisis de observaciones en rayos-X en múltiples épocas durante 18 años de la SN 1996cr, una de las cinco SNe más cercanas detectados en la época moderna. Observaciones de *Chandra* HETG en 2000, 2004 y 2009 nos permiten resolver espectralmente los perfiles de velocidad de líneas de emisión de Ne, Mg, Si, S y Fe, así como monitorear su evolución como trazadores de la interacción ejecta-CSM. Para explicar la diversidad de líneas de emisión en rayos-X exploramos algunos posibles modelos geométricos. Basados en las observaciones del 2009 con alta señal-ruido, encontramos que una geometría polar con una configuración de dos distintos ángulos de apertura y obscuración interna puede exitosamente reproducir todos los perfiles de líneas observados. Ajustamos modelos que consideran la convolución de los modelos geométricos con plasmas sin-equilibrio simples y dobles con componentes de absorción a la época 2009. Encontramos que el mejor modelo obtenido consiste de dos plasmas. Una componente es ligeramente absorbido ($2 \times 10^{21} \text{ cm}^{-2}$), plasma frío ($\approx 2 \text{ keV}$) con altas abundancias de Ne, Mg, Si y S, y asociada con una región de interacción polar extendida (ángulo de semiapertura $\approx 58^\circ$). Mientras que la otra componente tiene absorción moderada ($2 \times 10^{22} \text{ cm}^{-2}$), un plasma caliente ($\sim 30 \text{ keV}$) con abundancia de Fe alta y fuerte absorción interna, asociada con una región de interacción fuertemente polar (ángulo de semiapertura $\approx 20^\circ$). Extendemos este modelo a otras siete épocas con baja señal-ruido y/o baja resolución espectral (*XMM-Newton* en 2001, 2013, 2014, 2016 y 2018), produciendo varias tendencias interesantes. El flujo, el cual es siempre dominado por el plasma caliente, alcanzando un punto máximo entre 2004–2009 y actualmente disminuyendo, indicando que la onda de

choque esta pasando a través de un CSM de densidad más baja (viento de una gigante roja), de acuerdo con simulaciones hidrodinámicas previas. Las temperaturas del plasma y la velocidad de expansión muestran disminuciones suaves según las expectativas, mientras que las abundancias muestran aumentos leves, sugiriendo posibles influencias del material eyectado. Discutimos las implicaciones físicas de estos resultados y su impacto para identificar potenciales progenitores.

Abstract

We present X-ray spectra spanning 18 years for SN 1996cr, one of the five nearest SNe detected in the modern era. *Chandra* HETG exposures in 2000, 2004, and 2009 allow us to resolve spectrally the velocity profiles of Ne, Mg, Si, S, and Fe emission lines and monitor their evolution as tracers of the ejecta-circumstellar medium (CSM) interaction. To explain the diversity of X-ray line profiles, we explore several possible geometrical models. Based on the highest signal-to-noise 2009 epoch, we find that a polar geometry with two distinct opening angle configurations and internal obscuration can successfully reproduce all of the observed line profiles. We convolve our geometric models with single and double temperature absorbed non-equilibrium plasmas to fit the complete 2009 epoch spectrum. We find the best-fit model consists of two plasma components. One is mildly absorbed ($2 \times 10^{21} \text{ cm}^{-2}$), cooler ($\approx 2 \text{ keV}$) with high Ne, Mg, Si, and S abundances associated with a wide polar interaction region (half-opening angle $\approx 58^\circ$). The other is a moderately absorbed ($2 \times 10^{22} \text{ cm}^{-2}$), hotter ($\sim 30 \text{ keV}$) plasma with high Fe abundances and strong internal obscuration associated with a narrow polar interaction region (half-opening angle $\approx 20^\circ$). We extend this model to seven further epochs with lower signal-to-noise ratio and/or lower spectral-resolution (*XMM-Newton* in 2001, 2013, 2014, 2016 and 2018), yielding several interesting trends. The flux, which is always dominated by the hotter plasma, peaked between 2004–2009 and now is declining, indicating that the shock is now passing through a lower density CSM (red giant wind), in agreement with previous hydrodynamical simulations. The plasma temperatures and expansion velocity show mild declines in line with expectations, while the abundances show mild increases, suggesting

possible influences by the ejecta. We discuss the physical implications of our results and their impact for identifying potential progenitors.

Chapter 1

Introduction

Core-Collapse supernovae (CCSNe) are among the most powerful astrophysical events and are generated by the explosion of massive stars, $M > 8M_{\odot}$ (Woosley et al. 2002; Branch & Wheeler 2017). They are a fundamental component in the evolution of the Universe because they enrich the interstellar medium with heavy elements (Silicon, Sulfur, Magnesium, Iron, etc.) that are critical for the formation of new generations of stars and planets. At the same time, these events provide a new window to study the still poorly understood physical processes that occur during the final stages of the lives of massive stars.

1.1 General features of SNe type IIn

Type IIn SNe are a relatively rare subclass of CCSNe (less than 10% of the total number of CCSNe; Eldridge et al. 2013) which exhibit strong narrow –tens to hundreds of km s^{-1} – and/or intermediate-width –a few thousands of km s^{-1} – emission lines of Hydrogen or Helium in their optical spectra (e.g., Schlegel 1990; Filippenko 1997). Usually, they are associated with explosions that occur in dense circumstellar media (CSM; $n \gtrsim 10^{6-8} \text{ cm}^{-3}$), which were produced by stellar winds and outflows during previous evolutionary phases. The progenitors of SNe IIn are typically thought to have mass-loss rates of the order of

$\dot{M} \sim 10^{-4} M_{\odot} \text{ yr}^{-1}$ in the decades prior to explosion (Woosley et al. 2002).

Type II_n SNe are generally radio and X-ray bright, owing to a strong shock interaction between the ejecta and CSM (Branch & Wheeler 2017). The radio emission comes from non-thermal synchrotron emission, while X-rays arise from thermal processes. Moreover, because they are masked by strong ongoing CSM interaction (Smith et al. 2014), type II_n SNe rarely exhibit a classical nebular phase (when SNe enter the nebular phase, they reveal spectral fingerprints of their deep interiors, glowing by radioactivity produced in the explosion; Jerkstrand 2017) with a clear radioactive decay tail (Branch & Wheeler 2017). Furthermore, SN II_n show a long, slow decay in their optical light curves. The rapid decline rates can range from 0.03 to 0.07 mag d⁻¹ (Branch & Wheeler 2017), with the latter approaching the high rate of decline of SN IIP during the plunge from the plateau.

The basic scenario put forth to explain the multi-wavelength emission from CCSNe in general is that the SN explodes into a CSM formed by the stellar wind of the progenitor star (i.e., Region 1 of Figure 1.1; taken from Bauer et al. (2008)). A simple assumption is that the CSM has a radial power-law density profile r^s , where $s=0$ implies a constant density medium, $s=2$ implies a constant wind, and other values imply that the mass-loss parameters of the wind change with time. The ejecta, on the other hand, will have a very steep density profile (e.g., $\propto r^n$ where $n \sim 9$). The interaction between the ejecta and the CSM generates a forward shock (FS) that is driven outward inside the CSM and a corresponding reverse shock (RS) which is driven back into the SN ejecta. Under several simplifying assumptions, the shocks are expected to propagate in a "self-similar" manner (Chevalier 1982b).

The above scenario delineates four zones of material (these regions are enumerated as such in Fig. 1.1 *top left* corner): (1) the unshocked CSM outside the FS, (2) a shell of swept-up CSM that has been shocked by FS, (3) a shell of decelerated SN ejecta that has encountered the RS, and (4) the freely expanding SN ejecta. Between the FS and RS lies a region which separates the shocked ejecta and the shocked CSM known as the contact discontinuity (CD) (Chevalier 1982a; Bauer et al. 2008). At relatively early times, the shell

of shocked CSM will have a temperature of $T \sim 10^9$ K, while the shell of shocked ejecta is denser and cooler with a temperature $T \sim 10^7$ K (Bauer et al. 2008; Chandra 2018). The FS and shocked CSM are thought to give rise to radio, UV, and hard X-ray emission, while the RS and shocked ejecta provide the bulk of the soft X-ray emission (Bauer et al. 2008). A more detailed explanation can be found in: Smith (2016), Bauer et al. (2008), Chandra (2018) or Branch & Wheeler (2017).

Type IIn SNe are known to be radio and X-ray bright, mainly from regions (3) and (4) explained above, owing to a strong shock interaction between the ejecta and an exceptional dense CSM, which drives up the emissivity. That being said, while more than ~ 400 SNe IIn have been identified optically, only roughly a dozen or so are close enough or have a strong enough interaction to be observable with current X-ray instruments (Ross & Dwarkadas 2017; Chandra 2018).

1.2 SN1996cr

We focus here on the nearby SN 1996cr, which was initially discovered in the disk of the Circinus Galaxy by *Chandra* (Sambruna et al. 2001; Bauer et al. 2001) and later observed as a type IIn (Bauer et al. 2008), although its explosion epoch is only loosely constrained between 1995-02-28 and 1996-03-16, and its type at early epochs is yet to be established. SN 1996cr has remained bright at X-ray, optical, and radio wavelengths for nearly two decades, placing it amongst the remarkable handful of long-lived CCSNe attributed to strong ejecta-CSM interactions: e.g., SNe 1978K, 1979C, 1986J, 1988Z, 1993J, 2005kd, 2007bg, 2010jl, 2009ip, 1998S, and 1987A (e.g., Chandra et al. 2012b; Smith et al. 2014; Leonard et al. 2000; Dwarkadas et al. 2016; Margutti et al. 2017; Michael et al. 2002; Salas et al. 2013; Zhekov et al. 2006; Dewey et al. 2008). Due to its relative proximity to us of $d \approx 3.7$ Mpc, SN 1996cr affords us an exceptionally fantastic opportunity to study its features (Bauer et al. 2008; Dwarkadas et al. 2010; Dewey et al. 2011; Meunier et al. 2013) and evolution in great detail.

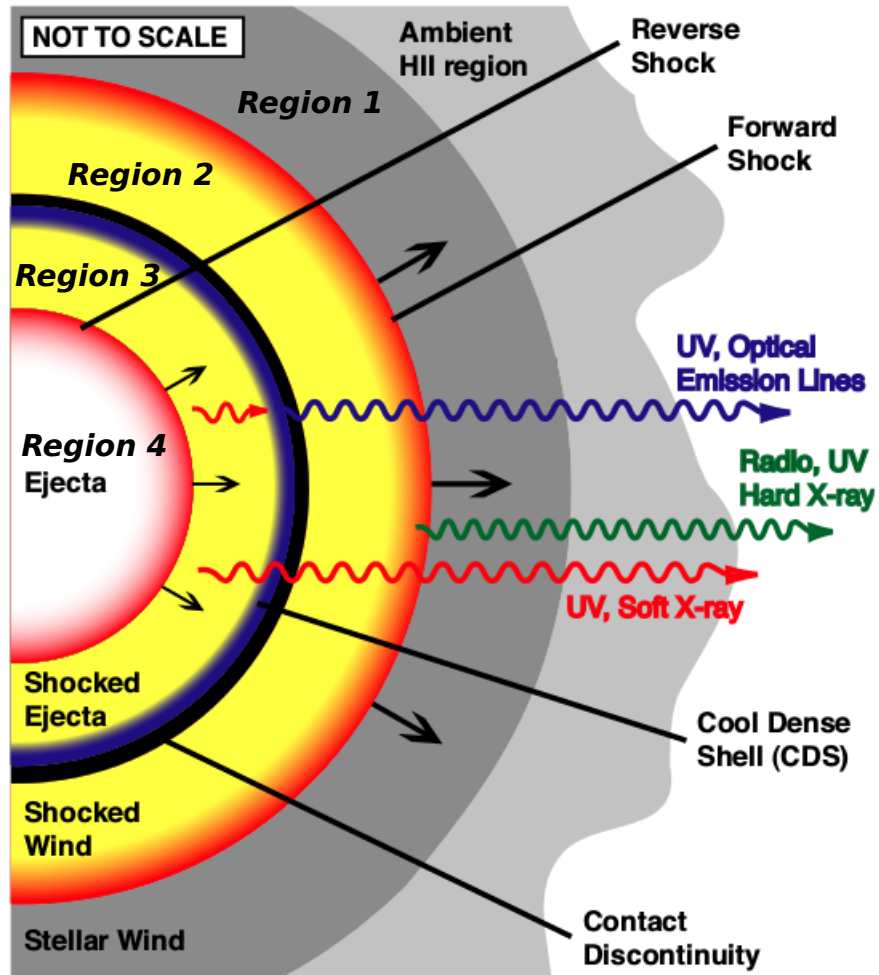


Figure 1.1: One-dimensional cartoon scenario of the CCSNe explained in § 1.1. Four different zones are noted with numbers: (1) unshocked CSM, (2) CSM shocked by a forward shock, (3) SN ejecta shocked by a reverse shock, and (4) freely expanding SN ejecta. In between the shocked ejecta and shocked CSM lies a region known as the contact discontinuity (CD), as well as a dense shell of cool material immediately behind it. Image reproduced from Bauer et al. (2008). Not to scale.

SN 1996cr’s radio emission shows an initial rise which is attributed to a combination of increasing CSM density and decreasing free-free absorption, which provides estimates of the CSM free electron density and hence insight into the ionization of SN 1996cr’s CSM (Meunier et al. 2013). The X-ray luminosity, likewise, exhibits an initial increase with time, only seen previously in the notable SN 1987A (e.g., Michael et al. 2002; Frank et al. 2016). This particular tendency, both in the radio and X-ray bands, is best explained by the interaction of ejecta material with a strong density enhancement (i.e., a dense shell) in the CSM (Michael et al. 2002; Dewey et al. 2008); Figure 1.2 compares SN 1996cr’s X-ray light curve to several other type II_n SNe and SN 1987A (multiplied by 10^3 for easier comparison). The luminosity data used in Fig. 1.2 is a literature compilation with distinct energy ranges; SN 1996cr and SN 1987A are shown for 0.5–2.0 keV, while SN 2010jl and SN 2006jd, are for 0.2–10.0 keV. The X-ray data for SN 1996cr and other young SNe II_n are available in the Supernova X-ray Database ¹ (SNaX, Ross & Dwarkadas 2017) and Immler et al. (2005, SN 1979C).

The optical spectrum of SN 1996cr similarly suggests that its progenitor was likely a massive star which shed several solar masses prior to the explosion. Additionally, the broad, high-velocity, multi-component Oxygen line complexes –in the optical range– hint at a possible concentric shell or ring-like morphology arising from the interaction of the forward shock and a dense shell produced by a wind-blown bubble (Bauer et al. 2008). These unparalleled features supported a deep *Chandra* campaign (PI Bauer) to obtain high resolution X-ray spectra taken between December 2008 and March 2009.

Using hydrodynamical simulations to model the X-ray light curve and spectrum at different epochs, Dwarkadas et al. (2010, hereafter D10) constrained the surrounding CSM structure of SN 1996cr, demonstrating that it exploded into a low-density medium, in contrast to the canonical picture of CCSNe (see above, which includes type II_n), before interacting with a dense shell of material located at a distance of $d \lesssim 0.03$ pc (three times smaller than SN 1987A’s ring; Dewey et al. 2012). This dense CSM shell likely

¹<http://kronos.uchicago.edu/snex/>

formed due to the interaction of a fast Wolf-Rayet (WR, $M > 30M_{\odot}$) or SN 1987A-like blue supergiant (BSG, $M > 15\text{--}20M_{\odot}$) wind ($\dot{M} \sim 10^{-5}\text{--}10^{-4}M_{\odot}\text{yr}^{-1}$; Crowther 2007), which turned on $\gtrsim 10^3\text{--}10^4$ yrs prior to explosion, and plowed up a previously existing red supergiant (RSG) wind ($\dot{M} \sim 10^{-4}M_{\odot}\text{yr}^{-1}$).² Under this scenario, SN 1996cr should have presumably exploded as a SN type Ib/c or II peculiar (e.g. Stockdale et al. 2009; Margutti et al. 2017). Other SNe or SNe remnants apparently exploded within a wind-blown bubble such as Cassiopeia A (Borkowski et al. 1996), RCW 86 (Vink et al. 1997) and Cygnus Loop (Levenson et al. 1997), for instance.

In this thesis, we revisit the X-ray spectral analysis of SN 1996cr, focusing in particular on the unique high spectral resolution and high signal-to-noise data acquired by *Chandra* over the past two decades. The detailed velocity structure of strong X-ray emission lines detected in this object provide a window into the processes of young SNe and allow us to probe the ejecta dynamics and abundances with great detail (e.g., Dewey et al. 2011, 2012; Katsuda et al. 2014). We initially consider different geometrical and physical scenarios to explain the 2009 *Chandra* data, which offers the highest signal-to-noise and hence the firmest constraints. We then explore the physical nature and evolution of the SN by applying our best fit scenario to high-quality X-ray observations at other epochs (2000, 2001, 2004, 2013, 2014, 2016, 2018) obtained by *Chandra* and *XMM-Newton*. Until now, only SN 1987A (and to a much lesser extent SN 1993J due to non-grating spectra) has had high resolution X-ray spectroscopic campaigns using *Chandra* or *XMM-Newton* (Michael et al. 2002; Zhekov et al. 2006; Dewey et al. 2008; Sturm et al. 2010). The outline of this thesis is as follows: Chapter §2 presents the data reduction; Chapter §3 explores how we build our source model, the physical implications, and the results from applying it to the 2009 and other epochs; Chapter §4 explains the main outcomes and their interpretations to constrain its nature; and finally, Chapter §5 presents our conclusions, final comments and future work.

²A luminous blue variable (LBV) stage was disfavored but could not be completely ruled out (Dwarkadas et al. 2010).

Following Bauer et al. (2008), we assume that the Circinus Galaxy is observed through a Galactic ‘window’ with a neutral hydrogen column density of $N_{\text{H}}=(3.0\pm 0.3)\times 10^{21}\text{ cm}^{-2}$, with possible additional internal obscuration (Schlegel et al. 1998; Dickey & Lockman 1990; Bauer et al. 2001). Similar to D10, we assume an explosion date of 1995.4 for SN 1996cr throughout this thesis. Errors are quoted at $1\text{-}\sigma$ confidence unless stated otherwise.

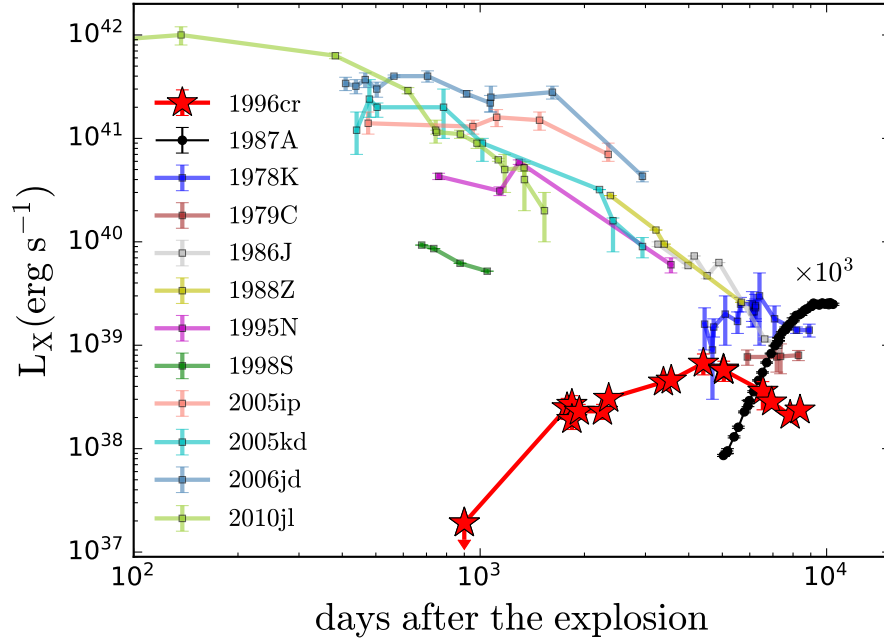


Figure 1.2: Representative X-ray light curves for a handful of type IIIn SNe (colour points), SN 1987A (black points, multiplied by 10^3) and SN 1996cr (*red stars*). The data were taken from Ross & Dwarkadas (2017) and Immler et al. (2005) (SN 1979C), with additional points added for SN 1996cr from *XMM-Newton*; no attempt has been made to regularize the X-ray band in which the luminosities from each SN are reported (e.g, some are reported as 0.5–2.0 keV, while others as 2.0–10 keV). The SNe appear to separate around 1000 days into early and late emitters. While several famous type IIIn SNe start out strong and fade with time, SN 1996cr increases with time, much like SN 1987A. SNe 1978K and 1979C may have had a similar evolution, as both exhibit flat X-ray evolution at late times, but lack early constraints to distinguish them as such.

Chapter 2

Data analysis

We use data obtained between 2000 and 2018; ergo, 5 to 21 years after the explosion, respectively, taken by the *Chandra* X-ray Observatory (CXO; Weisskopf et al. 2002) and the *X-ray Multi-mirror Mission (XMM-Newton)* (Jansen et al. 2001). We describe the processing and data reduction of each below.

2.1 Chandra X-ray Observatory

As we are principally interested in modeling the high signal-to-noise, high spectral resolution data, we focus on the available *CXO* data taken using the High-Energy Transmission Grating (HETG; Canizares et al. 2005), dispersed onto the Advanced CCD Imaging Spectrometer S-array (ACIS-S; Garmire et al. 2003); see Table 2.1. The HETG instrument consists of the High Energy Grating (HEG) and the Medium Energy Grating (MEG) assemblies, which operate simultaneously and have spectral resolutions of 0.7–80 eV (for 0.8–10.0 keV) and 0.5–70 eV (for 0.4–8.0 keV), respectively. The gratings have different energy-dependent effective areas, such that the MEG is generally more efficient for observing lower energy lines ($\lesssim 3$ keV) while the HEG better for higher energy ones ($\gtrsim 3$ keV). The gratings disperse a fraction of incident photons along dispersion axes offset by 10 degrees, such that the first and second orders of the HEG and MEG form a narrow

X-shaped pattern on the ACIS-S detector (Michael et al. 2002). (see Fig. 2.1 *top and medium panels*). Roughly half of the photons pass through the gratings undispersed (preferentially higher-energy photons) and comprise the HETG 0th order image on ACIS-S, with a spectral resolution of 100–170 eV between 0.4–8.0 keV (see Fig. 2.1, *top panel CCD S3*). For completeness, we extracted the low-resolution, 0th order data and retained it to help reduce uncertainties on some of the parameters of our model. With respect to the HETG extraction, SN 1996cr is a point source and, due to the spatial and spectral photon selection, has negligible background and no obvious contamination from the AGN or other point source spectra (dispersed or undispersed).

The *Chandra* data were reduced using CIAO (v4.9) and corresponding calibration files (CALDB v4.7.4). After standard processing and cleaning, we extracted each HEG/MEG spectrum as follows. We resolve the spectral orders making use of the procedures `tg_create_mask` and `tg_resolve_events`, and create response files (ARF and RMF) for each spectral order using the `mktgresp` tool; we consider only the $m = \pm 1$ orders in this work. Finally, we combine spectra from the positive and negative orders and ObsIDs for each epoch using the script `combine_grating_spectra`. For the zero order data, we adopt source and background extraction regions with radii of 3.''44 and 9.''84, respectively, and use the `specextract` script to extract spectra and create response files, considering a point source aperture correction for the ancillary files. We combine the 0th order spectra with the `combine_spectra` script. To produce the 2009 epoch, we combined spectra between 2008-12-15 (ObsID: 10223) and 2009-03-01 (ObsID: 10873), for a total combine exposure of ~ 485 ks. For the 2000 epoch, we combine spectra for ObsIDs 374 and 62877 for a total exposure time of ~ 67.3 ks, while for the 2004 epoch, we combined ObsIDs 4770 and 4771 for a total exposure time of ~ 114 ks. See Table 2.1 for information on individual ObsIDs. In all cases, we confirm that the individual spectra do not change significantly over 3–6 month timescales, justifying their combination into the three epochs.

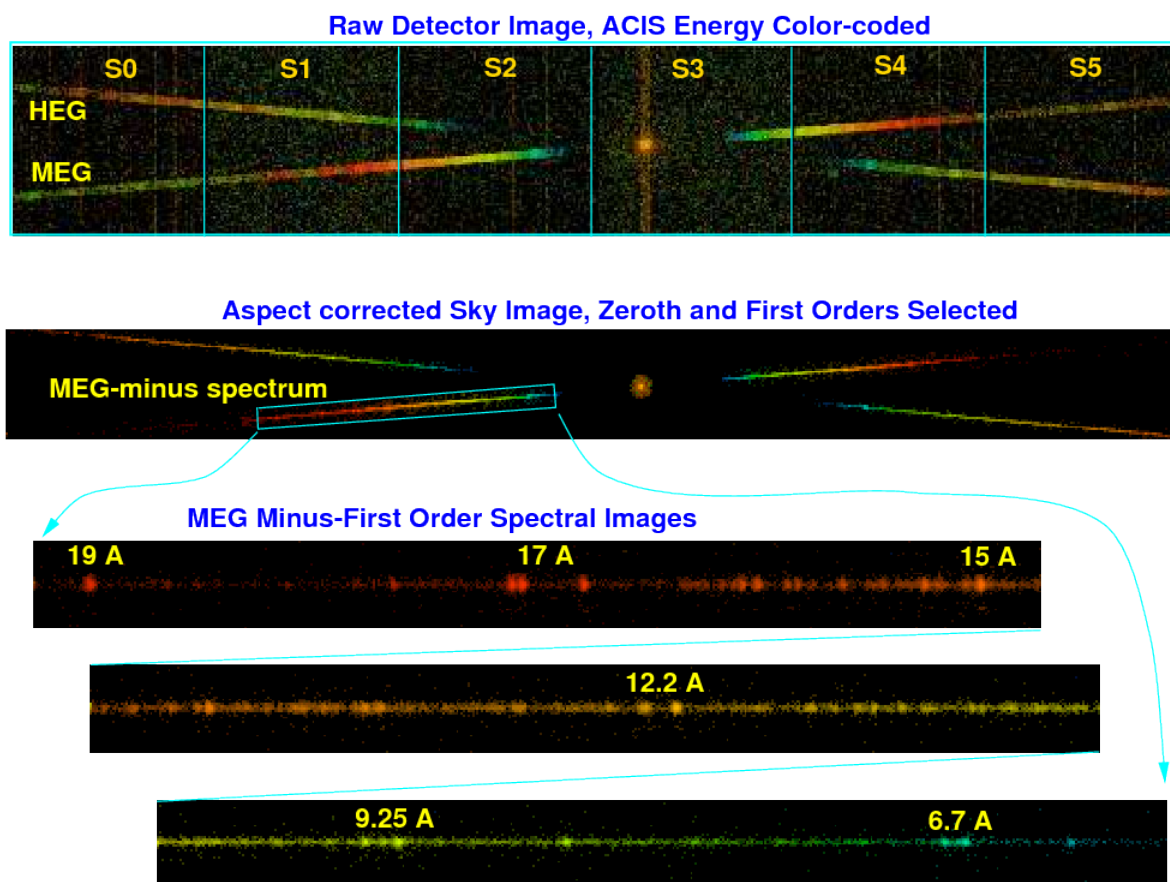


Figure 2.1: Example observation of a bright calibration target employing the HETGS-*CXO* instrument. The *top panel* shows an image of detected events on the ACIS-S detector, where colors indicate the ACIS-determined X-ray energy. The bright zeroth-order image is visible on CCD S3, while diffracted photons are visible forming a shallow X pattern where HEG and MEG spectra are indicated. The *middle panel* shows an image after the data have been corrected including only zeroth and first-order events. *Bottom panels* show an expanded view of the MEG minus first-order spectrum where emission lines are present. Figure adopted from The Chandra Proposers' Observatory Guide.

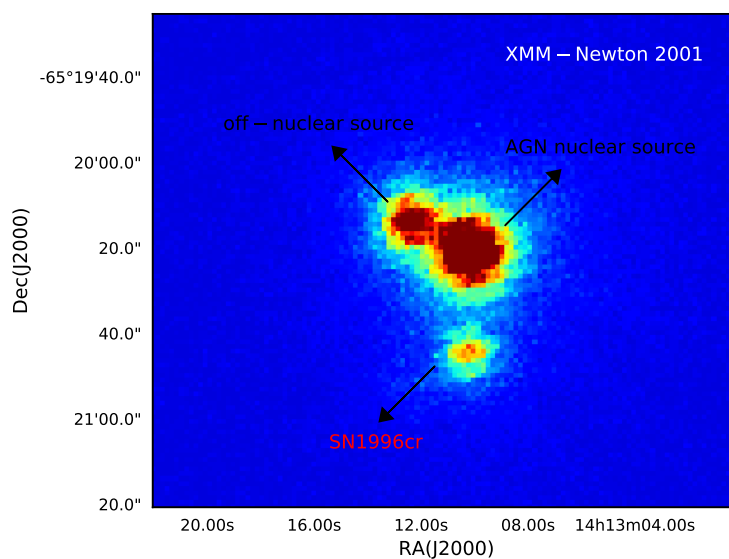


Figure 2.2: *XMM-Newton* (*pn*) SN 1996cr observation taken at the 2001 epoch. The emission features depicted are the AGN central point source, an off-nuclear point sources, and SN 1996cr. The faint extended emission from the central source provide an added background gradient across SN 1996cr.

2.2 *XMM-Newton*

To augment the *Chandra* spectra, we incorporate observations from *XMM-Newton* taken in 2001, 2013, 2014, 2016 and 2018. The *XMM-Newton* spacecraft consists of three X-ray telescopes with identical mirror modules, each equipped with a CCD camera which together comprise the European Photon Imaging Camera (EPIC; Strüder et al. 2001). Two of the telescopes employ Metal Oxide Semi-conductor (MOS; Turner et al. 2001) CCD arrays, installed behind Reflection Grating Spectrometers (RGS; den Herder et al. 2001) the MOS cameras only capture $\approx 44\%$ of the incident flux, after accounting for the $\approx 50\%$ diverted to the RGS detectors and structural obscuration. The third telescope focuses its unobstructed beam onto the *pn* CCD camera. The EPIC cameras provide sensitive imaging over a $\approx 30'$ field of view (FOV) in the 0.3–12.0 keV energy range, with modest spectral ($E/\Delta E \sim 20\text{--}50$) and angular (PSF, $\approx 6.''0$ FWHM) resolutions. This spectral resolution equates to velocities of $\gtrsim 6000\text{--}15000 \text{ km s}^{-1}$, such that the EPIC cameras are only able to marginally constrain the largest velocities seen from SN 1996cr (e.g., $\approx 4000\text{--}6700 \text{ km s}^{-1}$; Bauer et al. 2008). Thus, while the *XMM-Newton* epochs have insufficient resolution X-ray spectroscopy to constrain the velocity structure of the emission lines in the same way as the *CXO-HETG* spectra, they do provide useful constraints on the evolution of the continuum shape and line abundances of the SN. Table 2.1 shows exposure times for the *XMM-Newton* instruments at each epoch. Due to the poorer angular resolution of *XMM-Newton* and the relative position of SN 1996cr with respect to the bright AGN emission in the Circinus Galaxy, the spectra of SN 1996cr suffer some contamination from the central AGN. Thus, particular care must be taken to select a region for appropriate and optimal background subtraction.

Each epoch of *XMM-Newton* data was reduced using SAS (v16.1.0) package. After standard processing and cleaning, we extracted MOS1, MOS2, and *pn* spectra using a circular aperture of radius $8.''7$ centered in the SNe using the `xmmextractor` script. To select a background region which removes the substantial radially symmetric contamination

from the AGN (e.g., due to the point spread function and Thomson scattered reflection continua and Fe $K\alpha$ line emission; Arévalo et al. 2014), we adopted a half-annulus centered on the AGN with inner and outer radii of $16.''2$ and $33.''8$ (i.e., at a radial offset comparable to that of SN 1996cr from the nucleus), respectively, which excluded the extraction region of the SN itself and avoided the other bright off-nuclear source (Bauer et al. 2001) and ionization cone (Arévalo et al. 2014). In Figure 2.2, we show an image of the Circinus Galaxy for the 2001 epoch, taken by *pn*-camera on board *XMM-Newton*; the central AGN, as well as an off-nuclear source and SN 1996cr are indicated. Table 2.1 provides the observation ID, date, useful exposure time and instruments used in this work.

Table 2.1: X-ray observations used in this work, ordered by date, with each designated epoch separated by horizontal lines. *Column 1:* Observation ID. *Column 2:* UT date of observation. *Column 3:* Cleaned, useful exposure time. When three values are listed, these are for the MOS1, MOS2 and *pn* instruments, respectively. *Column 4:* X-ray instrument used.

ObsID	Date (UT)	Exposure (ks)	Instruments
374	2000-06-15	7.1	<i>Chandra</i> HETG
62877	2000-06-16	60.2	<i>Chandra</i> HETG
0111240101	2001-08-06	85.5/91.8/59.5	<i>XMM-Newton</i> MOS1/MOS2/ <i>pn</i>
4770	2004-06-02	55.0	<i>Chandra</i> HETG
4771	2004-11-28	59.5	<i>Chandra</i> HETG
10223	2008-12-15	102.9	<i>Chandra</i> HETG
10224	2008-12-23	77.1	<i>Chandra</i> HETG
10225	2008-12-26	67.9	<i>Chandra</i> HETG
10226	2008-12-08	19.7	<i>Chandra</i> HETG
10832	2008-12-18	20.6	<i>Chandra</i> HETG
10833	2008-12-22	28.4	<i>Chandra</i> HETG
10842	2008-12-27	36.7	<i>Chandra</i> HETG
10843	2008-12-29	57.0	<i>Chandra</i> HETG
10844	2008-12-24	27.2	<i>Chandra</i> HETG
10850	2009-03-03	16.5	<i>Chandra</i> HETG
10872	2009-03-04	13.9	<i>Chandra</i> HETG
10873	2009-03-01	18.1	<i>Chandra</i> HETG
0701981001	2013-02-03	47.8/49.0/36.4	<i>XMM-Newton</i> MOS1/MOS2/ <i>pn</i>
0656580601	2014-03-01	31.4/31.2/17.1	<i>XMM-Newton</i> MOS1/MOS2/ <i>pn</i>
0792382701	2016-08-23	19.8/19.6/17.0	<i>XMM-Newton</i> MOS1/MOS2/ <i>pn</i>
0780950201	2018-02-07	41.9/41.3/35.7	<i>XMM-Newton</i> MOS1/MOS2/ <i>pn</i>

Chapter 3

Methodology and Model

As shown in Figure 3.1, the intense, broad, asymmetric ionized emission lines in the 2009 epoch spectra of SN 1996cr are indicative of a strong ejecta-CSM interaction. CSM geometries have been revealed/inferred for a number of SNe to date. Most notable is the remarkable SN 1987A, for which a complex CSM ring was directly imaged (e.g., Michael et al. 2003; Park et al. 2006; Zanardo et al. 2013; Frank et al. 2016; Dewey et al. 2008). Others include, e.g., SNe 1979C, 1986J, 1997eg, 1998S, 1993J, 2005kd, 2006jc, 2006gy, 2008iz, 2010jl, 2011dh, and 2014C (e.g., Leonard et al. 2000; Smith et al. 2007; Foley et al. 2007; Hoffman et al. 2008; Bartel & Bietenholz 2008; Chandra et al. 2009b; Bietenholz et al. 2010; Martí-Vidal et al. 2011; Bietenholz et al. 2012; Katsuda et al. 2016; Kimani et al. 2016; Dwarkadas et al. 2016; Bartel et al. 2017; Bietenholz et al. 2018), many of which are classified as type II_n.

Notably, SN 1987A has remained bright enough, for long enough, to support several campaigns with high-resolution X-ray spectroscopy (Michael et al. 2002; Zhekov et al. 2006; Dewey et al. 2008; Sturm et al. 2010). With thermal plasma temperatures in the range $T \sim 0.5\text{--}2$ keV, SN 1987A primarily exhibits ionized lines from Nitrogen (N), Magnesium (Mg), Oxygen (O), Neon (Ne) and Silicon (Si), but lacks higher ionization lines like Sulfur (S), Argon (Ar), Iron (Fe) and Nickel (Ni). Spatially resolved spectral analysis of these lines found that they have thermal widths of $\sim 60\text{--}300$ km s⁻¹ and Doppler

broadening widths of $\sim 300\text{--}700 \text{ km s}^{-1}$ that trace out the two-shock structure (forward and reverse) moving through the equatorial ring, the outer HII region, and the inner ejecta (e.g., Michael et al. 2002; Dewey et al. 2008, 2011).

In our case, SN 1996cr additionally presents strong lines associated with the He-like (FeXXV K- α ; 6.7 keV) and H-like (FeXXVI Ly- α ; 6.9 keV) ions of Iron, which are not seen in SN 1987A but appear in other SNe such as SNe 1986J (Temple et al. 2005), 1998S (Pooley et al. 2002), 2010jl (Chandra et al. 2012b), 2006jd (Chandra et al. 2012a), 2009ip (Smith et al. 2014; Margutti et al. 2014), and 2014C (Margutti et al. 2017). Such strongly ionized Fe lines in X-ray spectra are generally a sign of an exceptionally hot, multi-phased plasma ($T \gtrsim 10 \text{ keV}$), and possibly a strongly enriched medium with super solar abundances, associated with ejecta-CSM interaction (e.g., Nymark et al. 2006; Margutti et al. 2017).

As with SN 1987A, our ultimate goal is to understand and interpret the geometrical and physical information that is encapsulated in the velocity profiles of the emission lines stemming from the ejecta-CSM interaction of SN 1996cr. The observed line profiles shown in Figures 3.1 and 3.2 are well-resolved compared to the native HETG resolution (e.g., $\sim 400\text{--}700 \text{ km s}^{-1}$ at 2 keV and $\sim 1500 \text{ km s}^{-1}$ at 6.0 keV) and show substantial broad, asymmetric structure (up to $\sim 5000 \text{ km s}^{-1}$). To elucidate the nature of this structure, we compare the high signal-to-noise X-ray spectra from the 2009 epoch to a few physically motivated models (§3.1). Then, once we arrive at a best model to explain the 2009 grating data, we apply it to the other epochs to investigate parameter evolution (§3.2).

To fit the spectra we utilized the X-ray software fitting package XSPEC v.12.8.2n (Arnaud 2004) using ATOMDB v.3.0.9 and Anders & Grevesse (1989) abundances.¹ Due to the low number of counts per bin for high resolution X-ray spectroscopy, and to retain the highest spectral resolution with which to resolve emission lines, we adopt maximum likelihood statistics for a Poisson distribution, the so-called Cash-statistics (C-stat Cash 1979) to find the best-fit model.

Unless stated otherwise, we consider typically a confidence interval of $1\text{-}\sigma$ for the

¹<http://www.atomdb.org/>

parameter errors. For each *Chandra* HETG epoch, we fit simultaneously both the HEG and MEG first-order spectra to improve the statistics during the process of finding best-fit parameters. The HETG 0th order spectra were incorporated after arriving at a set of best fit values, to increase the number of photons and constrain the parameter errors better. For each *XMM-Newton* epoch, we fit simultaneously the *pn*, MOS1, and MOS2 spectra to arrive at a best fit. For lower signal-to-noise or lower spectral resolution epochs, we freeze some poorly constrained parameters to improve the stability of the fits.

3.1 Epoch 2009

3.1.1 Single plasma component (M1)

The interaction of the SN blast wave with the CSM sets up forward and reverse shocks (e.g., Chevalier 1982b) behind which one can find the shocked CSM and shocked ejecta, respectively. These shocked plasmas can generate copious thermal X-ray emission (Chevalier 1982a), in proportion to the temperature, ionization state, and density of the plasma. As the blast wave is rapidly expanding, and the density of the plasma remains relatively low, the typical ionization equilibrium timescales are of order a few to thousands of years depending on the density of the medium, and hence the X-ray emission must be computed under non-equilibrium ionization (NEI) conditions (e.g., Borkowski et al. 2001; D10). For this purpose, we employ the XSPEC NEI model *vpshock*, a plane-parallel shocked plasma model (Borkowski et al. 2001). This model parametrizes the shock as a function of: electron temperature (kT_e); ionization time scale $\tau = n_e t$, where n_e is the electron density and t is the time since the plasma was shocked; individual atomic abundances for He, C, N, O, Ne, Mg, Si, S, Ar, Ca, Fe, Ni with respect to Solar; and normalization, which depends on the angular distance (D_A), redshift (z), and emission measure of plasma as $C(D_A, z) \int n_e n_H dV$ (Borkowski et al. 2001). We utilized the atomic database ATOMDB v.3.0.9 (Smith et al. 2001), which has been updated to include

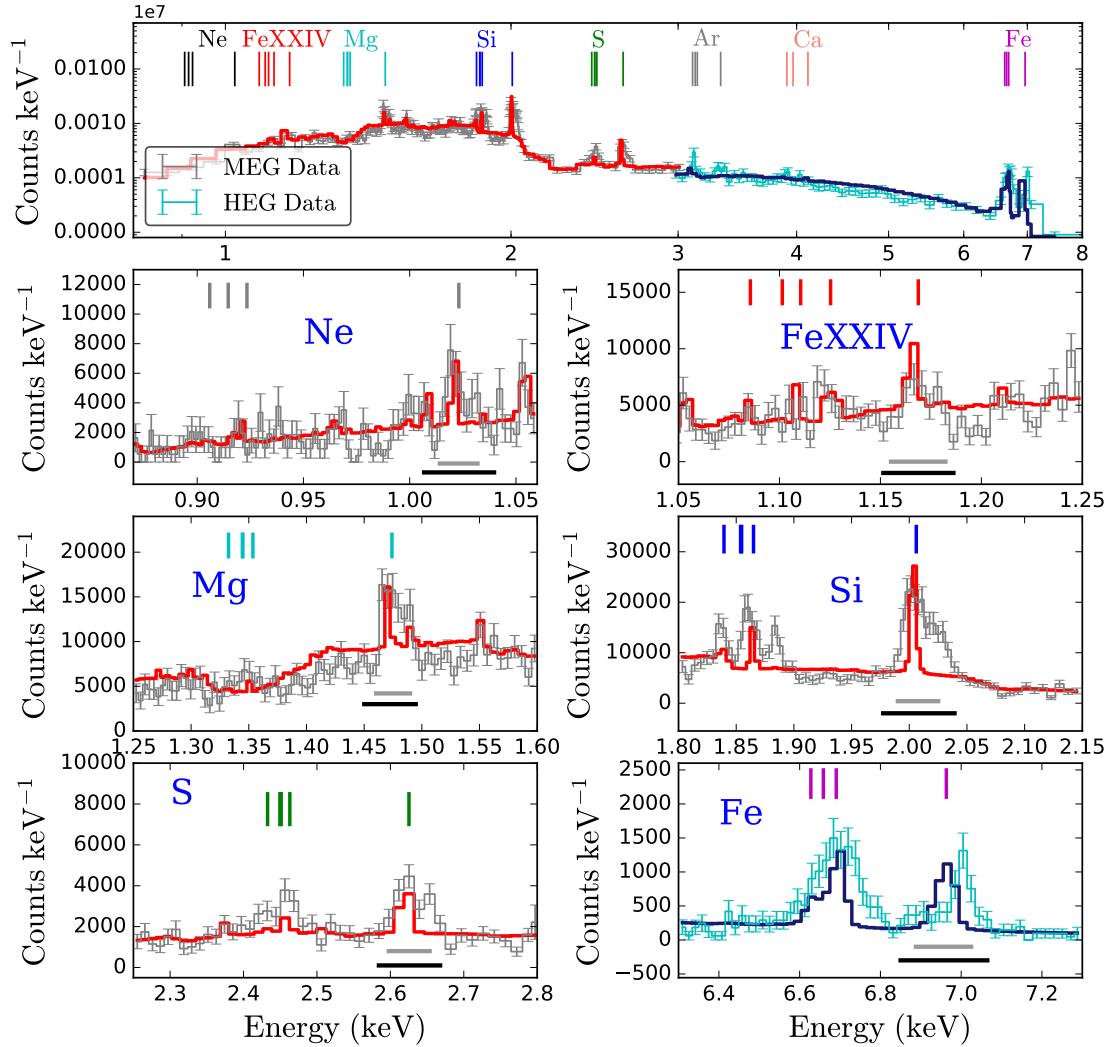


Figure 3.1: *Top panel:* Chandra HEG (cyan) and MEG (grey) X-ray spectra and $1\text{-}\sigma$ errors from the 2009 epoch, as well as blue and red solid lines representing the fitted model M1 (single plasma, no velocity structure) for the HEG and MEG, respectively. For clarity, we only show MEG/HEG below/above 3.0 keV. *Bottom panels:* close-up spectra of the H-like and He-like emission complexes for Ne, FeXXIV, Mg, Si, S and Fe. Vertical lines denote rest-frame energies. Horizontal grey and black bars represent line-widths of 3000 and 5000 km^{-1} , respectively, with respect to the H-like lines. While the bulk of the Fe XXVI emission is seen with velocity width $\lesssim 3000 \text{ km s}^{-1}$, other elements show substantial emission up to velocity widths of $\sim 5000 \text{ km s}^{-1}$, implying that Fe is produced from distinct regions respect the others.

relevant inner-shell processes that can be important for X-ray plasma spectral modeling of SN 1996cr.

We begin modeling process by fitting the 2009 epoch grating data with a single absorbed vpshock model at the systemic velocity (i.e., TBabs*vpshock; hereafter model M1). TBabs models the X-ray absorption due to the line-of-sight interstellar medium (ISM) (Wilms et al. 2000), parametrized by the equivalent hydrogen column, N_{H} ; this model adopts typical Milky Way ISM abundances, and incorporates interstellar grains and H_2 molecules. For M1, we model as free parameters kT_e , N_{H} , τ and the abundances of strong observed lines from Ne through Fe between 0.8–10.0 keV. In some cases, when we cannot constrain an elemental abundance well, we fix it to the solar value, under the assumption that the SN emission is highly enriched with heavy elements, in line with the results of D10. Other SNe like SN 1987A (Michael et al. 2002; Zhekov et al. 2009) or type IIn SN 2010jl, SN 2006jd, and SN 2005kd (Chandra et al. 2015; Dwarkadas et al. 2016; Katsuda et al. 2016) present similar high abundance values. The abundances of elements such as H, He, C, N, O, and Ni are always fixed to solar values, since their contributions are poorly constrained by the fitting process in this energy range.

For model M1, we find best-fit parameters of $kT_e = 13.4 \pm 0.9$ keV, $N_{\text{H}} = 3.9 \pm 0.2 \times 10^{21}$ cm⁻², $\tau = 8.1 \pm 1.3 \times 10^{12}$ s cm⁻³, and abundances ranging from 0.42–3.03 Z_{\odot} , with a C-stat of 10383.89 for 8545 degrees of freedom (DOF) (see Table 3.1). As seen in Figure 3.1, M1 provides a reasonable fit to the continuum (*top panel*) and approximates the intensity of the emission lines, but fails to model the Doppler width (~ 3000 – 5000 km s⁻¹) and line shapes (*bottom panels*), leaving large residuals. The H-like and He-like lines of other elements (e.g., Ne, Mg, S) suffer similar issues. We also note some residuals in the continuum fit between 4–6 keV, with the model being too high.

We can infer several things from the H-like and He-like Si and Fe profiles. First, the lines are resolved and asymmetric, which suggests they can provide critical insight on the kinematic sites of the ejecta-shock interaction(s). Such information has been previously inferred from 1-D hydro-dynamical modeling of SN 1996cr by D10, but not measured

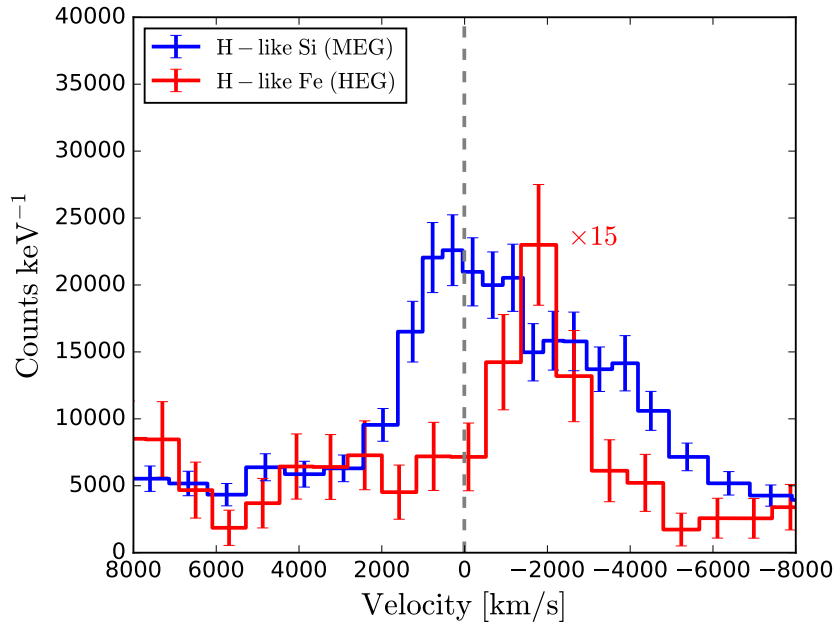


Figure 3.2: Comparison of the velocity profiles of the H-like Si (*blue* solid line) and Fe (*red* solid line) emission lines from the 2009 epoch, as detected by *Chandra*. The Fe counts have been scaled up by a factor of 15 to match better the Si counts. The profiles are clearly asymmetric and distinct.

directly. Moreover, the maximum velocities and shapes of the H-like Fe and Si profiles appear to be quite distinct. In Figure 3.2, we show the velocity profiles of H-like Si (*blue* line) and Fe (*red* line) for the 2009 epoch. The H-like Fe line appears to have a strong unresolved blueshifted peak and a $\sim 4\times$ weaker redshifted "peak" or "plateau", with maximum Doppler velocity offsets up to $\sim \pm 3000\text{--}4000 \text{ km s}^{-1}$ from the systemic host velocity. On the other hand, the H-like Si is much more centrally peaked around the systemic velocity, although it does show some signs of asymmetry favoring the blueshifted side, with Doppler velocities approaching $\sim \pm 5000 \text{ km s}^{-1}$ (see Fig.3.1). The other strong emission lines of Ne, FeXXIV, Mg, and S generally all show profiles comparable to Si. This maximum velocity and profile discrepancy between Fe and the rest of the elements suggests we are observing at least two kinematically and/or spatially distinct shocks.

3.1.2 Line Geometry

In the previous subsection, we discovered that the NEI-based model M1 provides a reasonable fit to the overall continuum and intensity (abundances) of elements, but fails to match the emission line profiles. We interpret this as a consequence of an expanding shock-interaction region. As a reasonable starting point, we assume that the density structure of both the ejected and surrounding material are spherically symmetric. To incorporate the resulting velocity structure into the NEI plasma models, we develop an XSPEC convolution model called 'shellblur',² which adopts a spherical geometry parameterized by a maximum velocity (v_{\max}), an inclination angle with respect to the line-of-sight (i), minimum and maximum polar angles (θ_{\min} , θ_{\max}),³ and an interior absorption term (N_{ejecta}). Interior to the reverse shock, we expect to find unshocked ejecta, which, if sufficiently dense, will absorb the shock emission on the (redshifted) farside. For simplicity, we assume a uniform unshocked ejecta density; a radially decreasing profile would tend to shift the velocity dependence of the absorption as well as make it more severe and abrupt. This convolution model allows us to infuse various geometrically motivated velocity profiles into our spectral fits. Figure 3.3 shows different geometrical interactions (*left panels*) and the corresponding line-profiles assuming a 6 keV emission line, a maximum expansion velocity of $v_{\max}=5000 \text{ km s}^{-1}$, an axis of symmetry inclined by 55° with respect to the line of sight and unshocked ejecta column densities of $N_{\text{ejecta}}=10^{20} \text{ cm}^{-2}$ ('unobscured'; *solid line*) and $N_{\text{H,ejecta}}=2 \times 10^{23} \text{ cm}^{-2}$ ('obscured'; *dashed line*). In Figure 3.4 we can see an illustration of the "shellblur" model considering a polar cap geometry ($\theta_{\max} = 90^\circ$ and $\theta_{\min} = 60^\circ$), for instance, and showing the configuration of its parameters associated with this particular geometry. The obscuring unshocked ejecta core inside the interaction region produces internal absorption of the shock emission from the farside. Also, the inclination angle (i) is measured from the line of sight to the polar axis. In Figure 3.5, we provide an example of how the velocity-profile changes as a function of line-of-sight inclination

²We make this available as a table model at <https://www.dropbox.com/s/ts1jfrg68nx38fo/>

³When $\theta_{\max}=90$, we can consider θ_{\min} to be the effective half-opening angle.

(different colors) for the latter two geometries [panels (c) and (d)] in Fig. 3.3. Here we convolve the geometric models with an unresolved Gaussian line centered at 6.0 keV and assume no internal absorption.

Assuming the shock interaction is ‘uniform’ and occurred in a geometrically thin, expanding shell, we should observe a square velocity profile (‘full shell’ scenario), as depicted in *panel a*) of Figure 3.3, convolved with model M1. However, if the density of the unshocked ejecta which is interior to the ejecta-CSM interaction region is high enough, then the receding side may be partially or fully obscured, effectively dampening the low-energy, redshifted portion of the profile. Both Si and Fe demonstrate this behavior, prompting us to also investigate a ‘full shell, obscured core’ scenario. Intriguingly, we observe neither of these basic ‘full shell’ scenarios, and rule them out at high confidence (see Fig 3.6 *top panels*; close-up of Mg, Si and Fe emission lines) because of high residuals. Instead, we observe more complex profiles from both the FeXXV/FeXXVI and lower energy lines. In the ‘full shell’ scenario convolved with M1, we obtained: $kT_e \sim 12$ keV, $N_H \sim 2.1 \times 10^{21}$ cm⁻² with a C-value of 8970.61 for DOF 8542. Keeping with the theme of symmetry, we next investigate toroidal and polar geometries. For the former we fix $\theta_{\min} = 0^\circ$, while for the latter we fix $\theta_{\max} = 90^\circ$.

With its resolved, pearl-necklace shock structure, SN 1987A is the most famous case for a ring-like or equatorial-belt geometry. The velocity profile associated with such morphology is a bullhorn shape, as depicted in *panel b*) of Figure 3.3. If we strongly obscure the emission from the (redshifted) farside of the model, the profile roughly mirrors that of FeXXVI (and less obviously the blended profile of FeXXV) in Fig. 3.2, although it remains difficult to fit the exact profile of both FeXXVI and FeXXV with any combination of line-of-sight angle, torus height, and interior obscuration due to the relative ratio of the blue/red peaks and the gap in between. The other lines are all too centrally concentrated, and strongly rule out a torus shape at high confidence (see Fig 3.6 *bottom panels*; close-up of Mg, Si and Fe emission lines) due to the high residuals in the H-like lines, mainly. In the ‘equatorial belt’ scenario convolved with M1, we obtained: $kT_e \sim 11.6$ keV, $N_H \sim 1.9 \times 10^{21}$

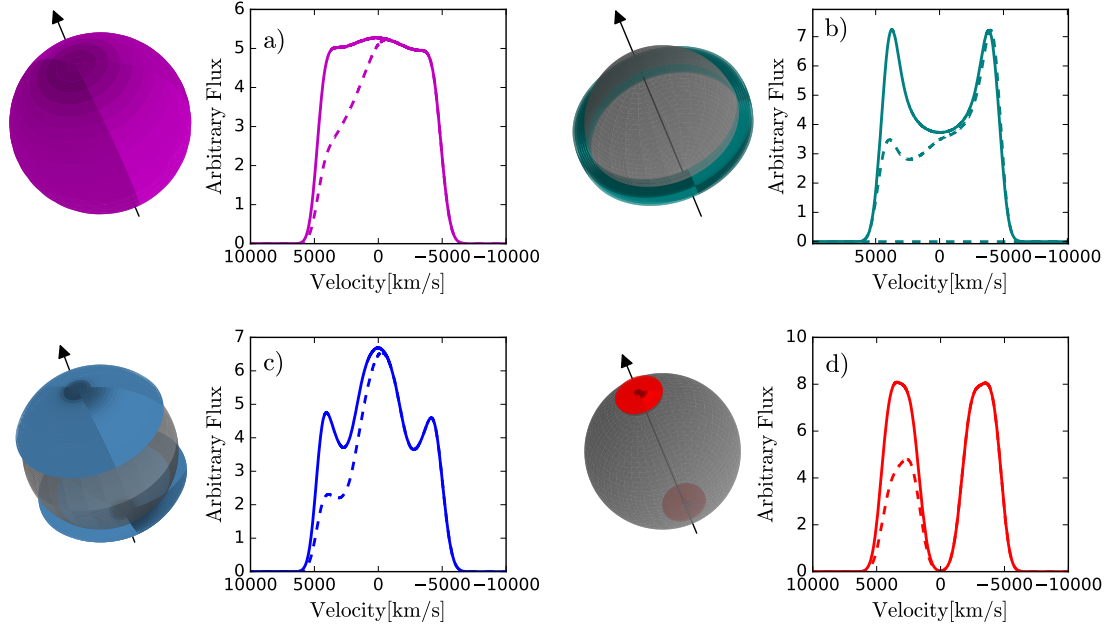


Figure 3.3: Examples of different expanding shock structure geometries, depicted by the colored regions in the *left panels*: (a) spherically symmetric; (b) a 10° -wide equatorial belt; (c) a 60° -wide polar cap; (d) a 20° -wide polar cap interaction. In all cases, we assume a maximum expansion velocity of $v_{\max}=5000 \text{ km s}^{-1}$, an axis of symmetry inclined by 55° with respect to the line of sight, and that there exists a uniform-density ejecta core which provides a maximum obscuration of up to N_{ejecta} (measured at the diameter) to the farside of the shock. The *right panels* show the resultant velocity profiles for each model assuming an input unresolved Gaussian emission-line centered at 6. keV. Two line-profiles are shown, one assuming $N_{\text{ejecta}}=1 \times 10^{20} \text{ cm}^{-2}$ (i.e., unobscured; *solid curves*) and another $N_{\text{ejecta}}=2 \times 10^{23} \text{ cm}^{-2}$ (i.e., obscured; *dashed curves*), to demonstrate the variety of profiles that can be generated by a given combination of geometry and internal absorber.

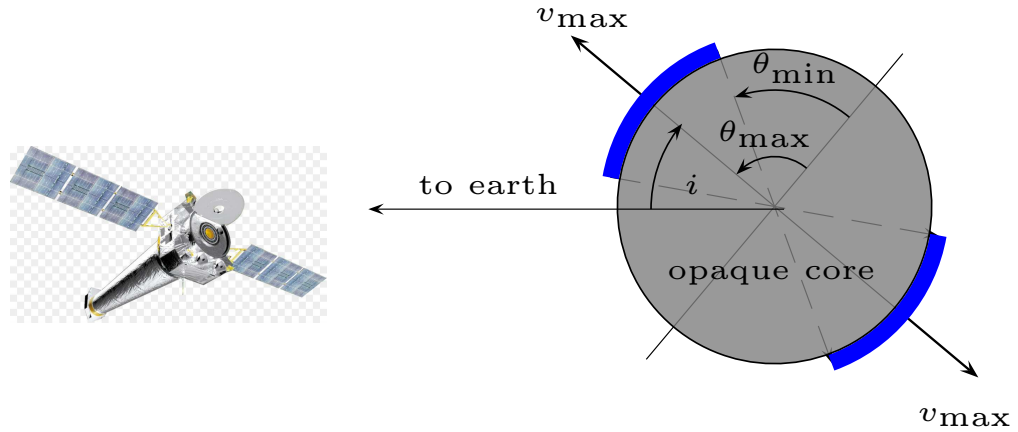


Figure 3.4: Illustration of the “shellblur” model showing the parameters’ configuration considering a polar cap expanding shock geometry. Both θ_{\max} and θ_{\min} define the aperture angle of the interaction region, while i is the inclination angle with respect to the line of sight and polar axis. Inside the expanding shock region, we can see the obscuring unshocked ejecta core which we assume absorbs emission from the far side, which we see in the redshifted part of the emission lines.

cm^{-2} with a C-value of 9120.94 for DOF 8542.

Another potential geometry for the shock interaction might be with a polar cap of a sphere. For example, the Homunculus Nebula around the luminous blue variable star (LBV) η Car (Smith 2013; Smith 2006; Smith et al. 2007; Davidson & Humphreys 1997). If η Car were to explode, the shock-interaction might develop primarily first along the equator and afterward along the polar axis due to the enhanced bipolar CSM density (van Marle et al. 2010). Depending on the opening angle of this polar emission and line-of-sight orientation angle, we could observe it either as a centrally dominant line, as depicted in *panel c*) of Figure 3.3, or even a widely spaced double Gaussian shape, as depicted in *panel d*) of Figure 3.3.

Figure 3.7 shows confidence contour maps for the strongest individual lines (*top panels*), considering polar geometry parameters θ_{\min} and i , and a comparison between them (*bottom panel*). We achieve good fits to the FeXXVI and FeXXV lines with relatively narrow opening angles ($\theta_{\min} \approx 60\text{--}75\text{deg}$), while the rest of the lines are well-fit with a wider

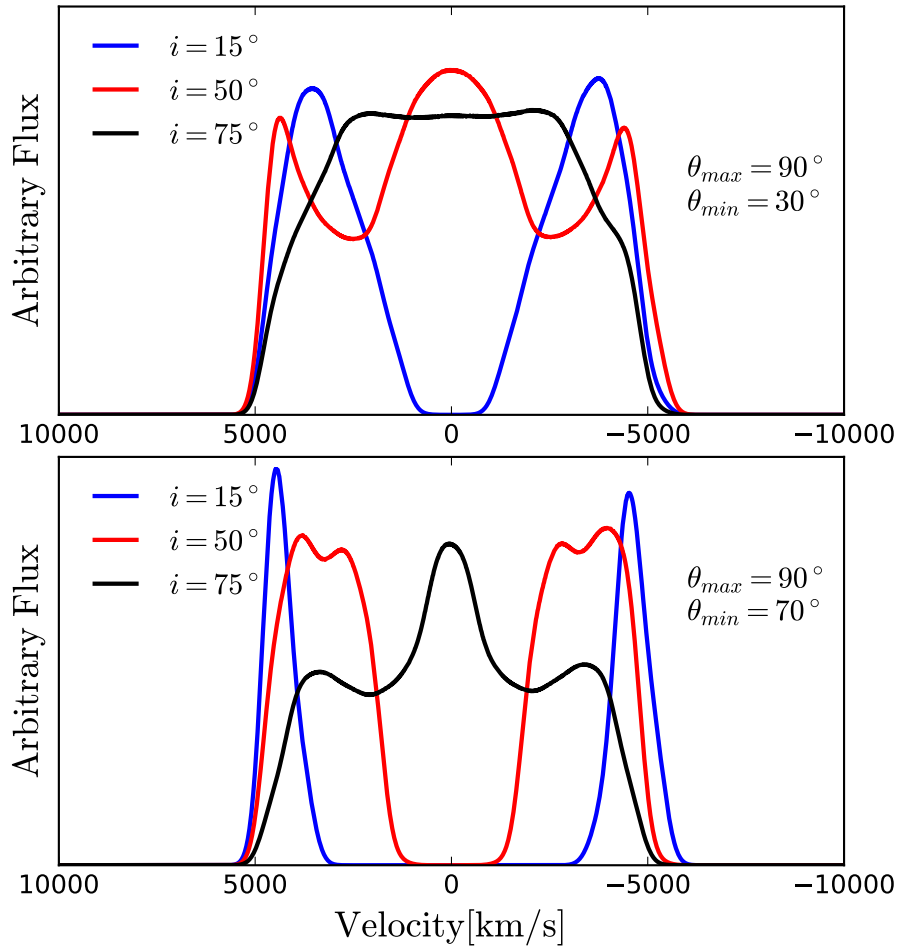


Figure 3.5: Comparison of velocity profiles as a function of line-of-sight inclination angles (15° , 50° , 75°) for the latter two geometries [panels (c) and (d)] in Fig. 3.3: wide polar angle ($\theta_{min} \sim 30^\circ$) in the *top panel* and narrow polar angle ($\theta_{min} \sim 60^\circ$) in the *bottom panel*. We convolved the above geometric models with an unresolved Gaussian emission-line centered at 6.0 keV, a maximum expansion velocity of $v_{max}=5000 \text{ km s}^{-1}$, and no internal obscuration.

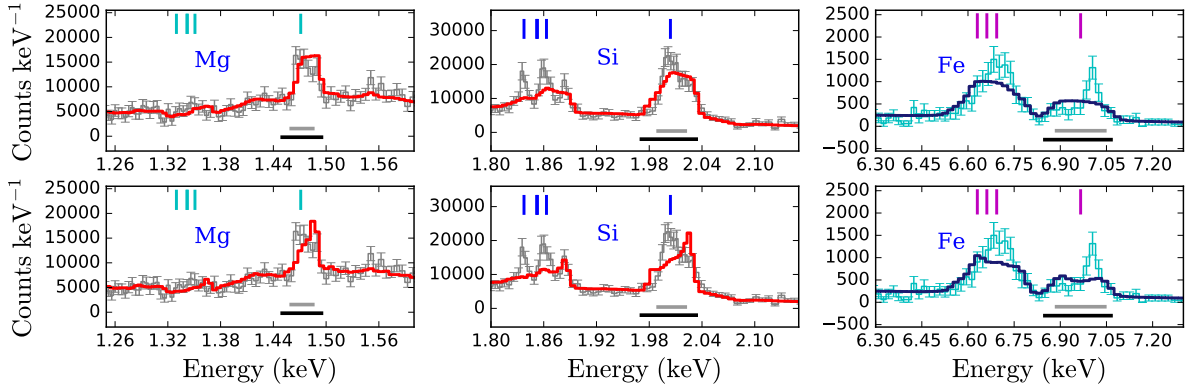


Figure 3.6: Close-up spectra of the H-like and He-like emission complexes for Mg, Si and Fe considering two scenarios: 'full shell-obscure core' (*top panels*) and 'equatorial-belt-obscure core' (*bottom panels*). Neither provides a good match.

polar angle ($\theta_{\min} \approx 25\text{--}35\text{deg}$). Intriguingly, the inclination angle i remains remarkably consistent across all individual line fits, at $\approx 55\text{deg}$. This suggests that the morphological alignment of most elements around the polar axis are, to first order, the same. The internal absorption and maximum velocity terms required for the lower energy lines were typically $\approx 2 \times 10^{22} \text{ cm}^{-2}$ and $\approx 4600 \text{ km s}^{-1}$, respectively, while for the FeXXVI line we found better fits with values of $\approx 5 \times 10^{23} \text{ cm}^{-2}$ and $\approx 3000 \text{ km s}^{-1}$, respectively. For a fixed inclination angle of 55deg , the FeXXVI emission is more tightly concentrated around the polar regions, in agreement with the preliminary results from Dewey et al. (2011).

Finally, we note that the $1\text{-}\sigma$ contours on the inclination angle i and minimum opening angle θ_{\min} highlight some interesting behavior. The contours for Si and S are securely centred around the best fit values, while the contours of Fe XXVI trace out a narrow band in $i\text{-}\theta_{\min}$ parameter space. Given the degeneracy between i and θ_{\min} for FeXXVI in Fig. 3.7, an alternative physical scenario for this line might be with $i \sim 80\text{--}90\text{deg}$, $\theta_{\min} \sim 90\text{deg}$, and $v_{\max} \sim 4600 \text{ km s}^{-1}$, such that all of the lines shared a similar maximum velocity rather than a similar inclination angle. In addition, the Ne, FeXXIV, and Mg transitions, while having best-fit values close to Si, show skewed low-level contours toward higher θ_{\min} and

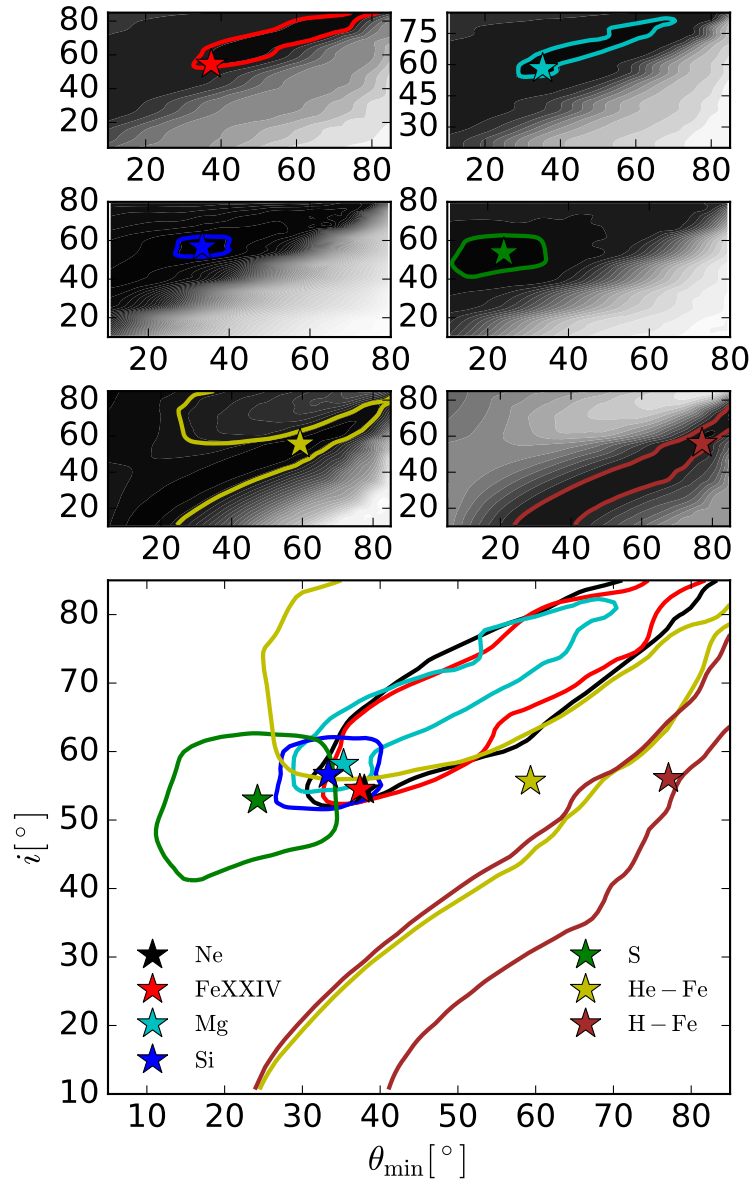


Figure 3.7: Error confidence contour maps, comparing the minimum polar angle (θ_{\min}) and line-of-sight angle (i) from the polar emission line model, for different emission lines in the 2009 *CXO* HEG/MEG spectra. *Top panels* show confidence contours with greyscale shading for the most intense individual lines, with lighter and darker colors representing higher and lower C-stat values, respectively. The solid color curves denote the 1- σ contours, while the stars are the best-fit values obtained. The *bottom panel* compares all of the 1- σ contours and best-fit values together.

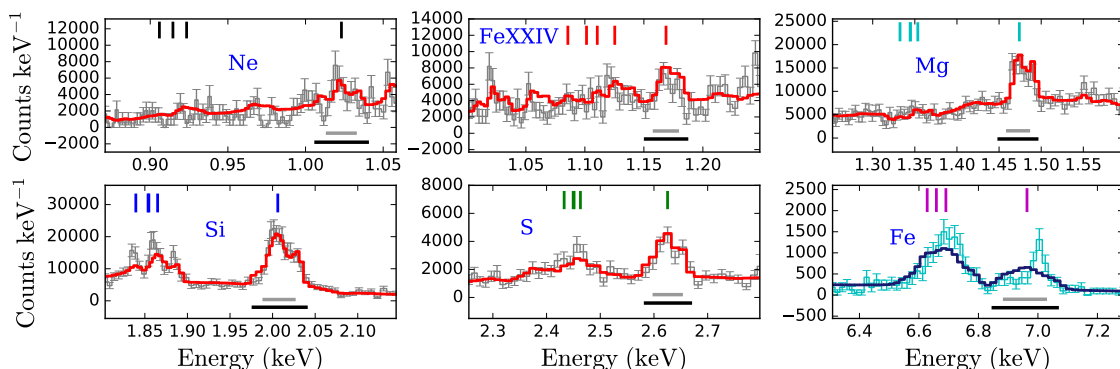


Figure 3.8: Close-up spectra of several well-detected H-like and He-like emission complexes from the 2009 *CXO* HEG/MEG spectra, overlaid with the fitted model M2 (single plasma, color emission). Colors and lines are the same as those presented in Figure 3.1. Model M2 provides a reasonable fit to the low energy lines, but fails to match the Fe line profiles. As in Fig. 3.1, horizontal grey and black bars denote line-widths of 3000 and 5000 km^{-1} , respectively, with respect to the H-like lines, highlighting the differences between the different lines.

i values. In contrast, the contours of FeXXV line exhibit best-fit contours sandwiched midway between the high (FeXXIV) and low (Si and S) solutions, with a large degenerate range of θ_{\min} and i values. Taken together, the contours of the various lines appear to reinforce the notion that there are at least two distinct components. The degeneracies between θ_{\min} and i are clear in Figure 3.5, which depending on the line-of-sight angle the line profiles take similar shapes for different opening angles.

To further understand the velocity profiles, we analyzed the contribution of the narrow $\sim 3000 \text{ km s}^{-1}$ FeXXVI component to lines below 4 keV . We began by fitting and removing such a component from the Ne, FeXXIV, Mg, Si, and S lines. This left as residuals a large central $FWHM \sim 1500 \text{ km s}^{-1}$ Gaussian component, a slightly smaller unresolved Gaussian offset by $\sim +5000 \text{ km s}^{-1}$, and in the case of S a third marginal unresolved Gaussian offset by $\sim -5000 \text{ km s}^{-1}$. Such residuals are not easily fit by any single geometric model as described above. We also highlight the remaining residuals in the He-like lines of Si, S, and Fe in §3.1.4. Both of these imply that further complexity (single or multiple

components) is likely required. We revisit this theme later in this section.

3.1.3 Single Plasma Component with Shellblur (M2)

Given the overall success of the polar geometry in arriving at a single inclination angle for all lines and relatively consistent best-fit parameters for the Ne, FeXXIV, Mg, Si, and S lines, we adopt it for the remainder of the analysis. We now return to the single temperature plasma model, convolving it with the polar geometry (i.e., TBabs*shellblur(vpshock); hereafter M2), and attempt a global fit of the 2009 epoch grating data.

A best-fit is obtained with the following geometrical parameters: $\theta_{\min} = 31^{\circ} \cdot 2_{-4.2}^{+4.6}$, $i = 56^{\circ} \cdot 1_{-2.3}^{+3.3}$, $v_{\max} = 4600_{-71}^{+71} \text{ km s}^{-1}$, $N_{\text{ejecta}} = 1.9_{-0.3}^{+0.3} \times 10^{22} \text{ cm}^{-2}$, $kT_e = 12.1_{-0.7}^{+0.9} \text{ keV}$, $N_H = 2.3_{-0.2}^{+0.2} \times 10^{21} \text{ cm}^{-2}$, $\tau = 4.4_{-0.1}^{+0.3} \times 10^{12} \text{ s cm}^{-3}$, and abundances ranging from 1.0–7.7 Z_{\odot} , with a C-stat value of 8910.25 for 8541 DOF.

As seen in Figure 3.8, model M2 yields a reasonable match to the strong lines of Ne, FeXXIV, Mg, Si and S, as well as the continuum (not shown), and results in a dramatic improvement in C-stat (see Table 3.1). However, it fails to fit the lines FeXXVI (~6.9–7.0 keV) and FeXXV (~6.7 keV), suggesting this model remains incomplete. This mismatch confirms our previous intuition that additional geometric/kinematic plasma components are needed.

3.1.4 Multiple Plasma Components with Shellblur (M3–M6)

We therefore develop a few more complex model combinations. First, we consider two NEI models with different temperatures, modified by a single foreground absorption and a shellblur term (TBabs*shellblur(vpshock+vpshock), hereafter model M3). The result is two independent best-fit temperatures of $kT_{e,1} = 10.6_{-0.5}^{+0.4} \text{ keV}$ and $kT_{e,2} = 0.9_{-0.1}^{+0.1} \text{ keV}$ and a column density of $N_H = 0.19_{-0.02}^{+0.02} \times 10^{22} \text{ cm}^{-2}$, which improves the residuals around the 4–6 keV continuum and lower energy lines somewhat compared to model M2, lowering the C-stat value to 8860.35 for 8538 DOF (see Table 3.1). In this

case, the hotter component dominates the total line and continuum emission, with the cooler component contributing a modest amount to the continuum shape below ~ 2 keV. Unsurprisingly, we find that the Ne, FeXXIV, Mg, Si, S lines are best-fit with geometric parameters similar to model M2, while the FeXXVI and FeXXV lines remain poorly fit. To limit the number of free parameters for model M3, the line-of-sight angle was fixed to the value of $55^\circ.0$ obtained previously from M2. Moreover, the abundances of H, He, C, N, O, Ar, Ca, Ni were fixed to solar values, while those of Ne, Mg, Si, S, Fe, as well as the ionization time scales and normalizations of both NEI models, were fit as free parameters. However, due to the overall dominance of the high-temperature component, only weak abundance constraints could be achieved in the low-temperature component. Given this, all of the abundance values between the low and high temperature components, except Fe, were tied together.

Next, we consider two NEI models with different temperatures and different geometric terms, all modified by a single foreground absorption term (TBabs(shellblur*vpshock+shellblur*vpshock), hereafter M4). The first shellblur*vpshock term is associated with a narrow polar cap (i.e., tracking FeXXVI), while the second shellblur*vpshock term is associated with a wider polar emitting region (i.e., tracking Ne, FeXXIV, Mg, Si, S). Somewhat surprisingly, if the plasma temperatures are left free, both tend toward values of $kT \sim 12$ keV absorbed by $N_H \sim 1.6 \times 10^{21} \text{ cm}^{-2}$, resulting in a C-stat value is 8858.40 for 8536 DOF (see Table 3.1). Thus this fit provides no clear improvement over model M3. The wide polar angle component dominates the overall continuum fit, with very marginal contribution from the narrow polar cap component. As with model M3, to limit the number of free parameters in model M4, we fix the line-of-sight angle to $55^\circ.0$, the values of ionization time scales to previous best-fit values, and the abundances of H, He, C, N, O, Ar, Ca, Ni to solar values and fit the abundances of Ne, Mg, Si, S, Fe abundances as free parameters, with all parameters aside from Fe tied together between components. Under reasonable Fe abundance assumptions, this model fails to match the FeXXVI and FeXXV lines well; to fit both H-like and He-like Fe line profiles requires abundances of

$Z_{Fe} \sim 250Z_{Fe\odot}$ in the narrow polar cap component and $Z_{Fe} \sim 0.54Z_{Fe\odot}$ in the wider angle component, respectively. So, we rule out model M4 to explain 2009 spectrum.

Up to this point, models M1–M4 have failed to fit the velocity profiles of all strong lines, especially the Fe ions. We next consider two NEI components with distinct temperature, geometry, and foreground absorption terms (TBabs(shellblur*vpshock)+TBabs(shellblur*vpshock), hereafter M5). The introduction of a second, higher absorption term coupled to the narrow polar cap plasma allows this component to contribute principally to the FeXXVI and FeXXV lines and the >4 keV continuum, while minimizing its role at lower energies. For the high absorption, narrow polar cap component (hereafter component 1, or C1), we fix the line-of-sight to $55^\circ.0$ and the abundances for elements $Z \leq 12$ to solar values (since this component is only dominant at >4 keV). For the low absorption, wider polar angle component (hereafter component 2, or C2), we fix the line-of-sight to $55^\circ.0$ and the abundances for elements $Z \leq 9$ to solar values. All other parameters in both components are left free. A best-fit is obtained with the parameters listed in Table 3.2, resulting in abundances ranging from 0.3–3.9 Z_\odot in Table 4.1 and a C-stat value of 8779.60 for 8528 DOF. This model provides a modest improvement over models M3 and a variable-Fe version of M4.

Figure 3.9 demonstrates that the best-fit M5 model results in reasonable fits to all of the strong lines in the 2009 epoch spectra. *Dashed* and *dotted* lines represent the C1 (high kT , high N_H , narrow polar angle) and C2 (low kT , low N_H , wide polar angle) components, respectively. Table 3.1 shows the C-statistic values corresponding to each model and their DOFs, demonstrating that M5 has the lowest C-stat value for the 2009 epoch.

Given that multiple temperature components are expected even in 1-dimensional shocks (e.g., D10), and that there appear to be two geometrically distinct shocks as traced by the line profiles, we are tempted to consider additional plasma components. To this end, we added an extra absorbed NEI model, both fixing its geometrical components to one of the previous polar scenarios (wide or narrow) as well as fitting the parameters freely. In none of these cases we find a statistically significant improvement with respect to model

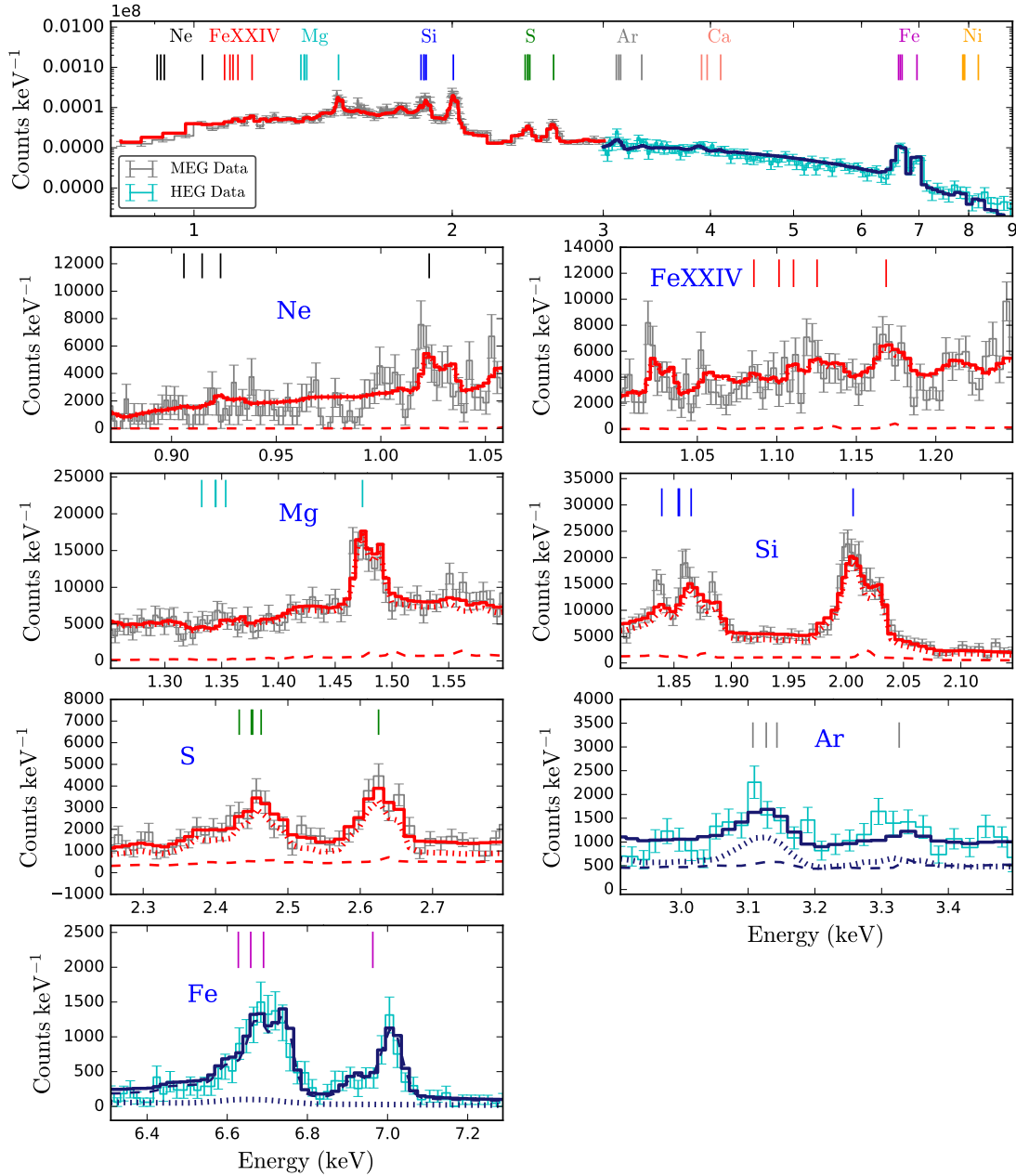


Figure 3.9: *Top panel:* Same as Fig. 3.1 but with the best-fitting model M5 (two temperatures, two polar geometries) compared to the 2009 epoch spectra. *Bottom panels:* Close-up spectra of all detected H-like and He-like emission complexes. Colors and lines are the same as those presented in Figure 3.1. MEG spectra are shown for Ne, FeXXIV, Mg, Si, and S line complexes, while HEG spectra are shown for Ar and Fe. Model M5 provides a reasonable fit to all of the lines.

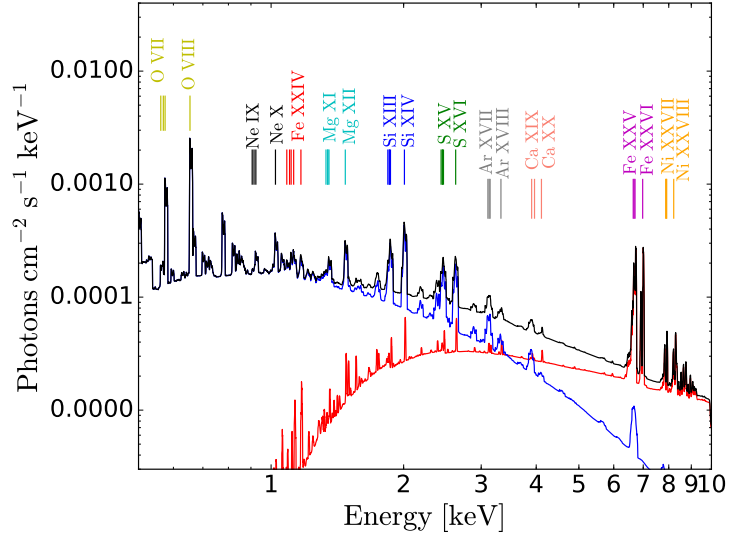


Figure 3.10: Best-fit model M5 spectrum (*black* line) between 0.3–10 keV in units of Photons $\text{cm}^{-2} \text{s}^{-1} \text{keV}^{-1}$. The higher and lower temperature components are denoted in *red* and *blue*, respectively. The color vertical lines mark the most intense lines of the H-like and He-like ions of high-Z elements.

M5, indicating that two dominant plasma components are sufficient to explain the physical nature of the SN shock.

Figure 3.10 shows the full M5 model (*black* curve) along with the individual high (C1) and low (C2) temperature NEI plasma components (*red* and *blue* curves, respectively) and the most important emission lines (vertical colored lines). To limit the C1 component from contributing to low-energy lines or dominating the continuum, it must be strongly absorbed ($2.5 \times 10^{22} \text{ cm}^{-2}$) compared to the C2 component ($1.7 \times 10^{21} \text{ cm}^{-2}$). In this scenario, the higher temperature, narrow polar component (*red*) contributes strongly to high-energy lines and underlying continuum of Fe and Ni, and modestly to mid-energy lines of S, Ar, and Ca, while the lower temperature, wider polar component (*blue*) contributes strongly to the low-energy lines and continuum of Ne, Mg, Si, FeXXIV, and modestly to mid-energy lines of S, Ar, and Ca. We note that the temperature, kT_e , in the hotter component is not well-constrained, owing to the HETG’s limited energy range and decreasing effective area

at high energies (see Table 3.2). While the best-fit value is $kT_e = 33.5$ keV, we obtain a $3\text{-}\sigma$ range spanning $\sim 10\text{--}80$ keV. The bright H-like and He-like Fe lines, which require a high degree of ionization, provide additional constraints on the temperature, although these are somewhat degenerate with abundance. Thus, it is crucial to have wide-band X-ray coverage to constrain the temperature of the SNe and disentangle instrumental and physical effects (e.g. SN 2010jl, Chandra et al. 2015; Chandra 2018). While *NuSTAR* observations covering the 3–79 keV range exist for the Circinus galaxy, due to their coarse spatial resolution the emission from SN 1996cr is severely contaminated by the much stronger AGN emission (see Figure 1 of Arévalo et al. 2014).

Given that the contours of the lower energy lines of Mg, Si, and FeXXIV skew toward higher θ_{\min} in Fig. 3.7, these lines may indeed have a potential contribution from the narrow polar component which is not being modeled with M5. Therefore, we consider one final scenario, in which the hotter polar component is only partially absorbed (TBabs(shellblur*vpshock)+TBpcf(shellblur*vpshock), hereafter M6). Model M6 introduces two additional parameters, the redshift z and a partial covering fraction PCF, and allows us to evaluate whether the narrow polar component contributes to emission lines below ~ 4 keV. We obtained a best-fit with model M6 yielding a C-value of 8785.95 for 8527 DOF, which is slightly higher than the best-fit for model M5. In addition, the PCF parameter converged to a value of 1, suggesting that the narrow polar component does not contribute significantly to emission lines below ~ 4 keV. Given the fitting results above, we do not include this result in Table 3.1 and consider model M5 to be the best and final model for the 2009 epoch (see Fig. 3.9).

3.2 2000, 2001, 2004, 2013, 2014, 2016 and 2018 epochs

Now that we have obtained a reasonable physical model for the 2009 epoch, we explore how the ejecta-CSM interaction in SN 1996cr may have evolved between years 5.5 and 22 post-explosion, effectively reconstructing its “history” using the other *Chandra* and

Table 3.1: Statistic values associated with each model for the 2000, 2004 and 2009 epochs (*CXO* observations). *Column 1* refers the model used, and *Columns 2, 3 and 4* contain the C-statistic and degrees of freedom values for each model and epoch.

Model	Cstat(dof)		
	2000	2004	2009
M1	4464.09(8546)	6543.35(8545)	10383.89(8545)
M2	4426.79(8542)	6300.97(8542)	8910.25(8541)
M3	4406.17(8540)	6290.69(8539)	8860.35(8538)
M4	4441.00(8538)	6331.96(8536)	8858.40(8536)
M5	4398.56(8533)	6264.33(8533)	8779.60(8528)

XMM-Newton epochs.

For the high-resolution 2000 and 2004 *Chandra* epochs, we apply models M1 through M5, fitting the geometry, temperature, absorption and abundance parameters in a similar manner as the 2009. We find that model M5 is the best-fitting model for both epochs, based on the C-statistic values (see Table 3.1). This consistency is reassuring, and give us confidence to trust the evolution of the freely fit parameters. Unfortunately, the errors on the parameters are generally larger due to the poorer photon statistics of these earlier epochs, and we fail to detect some line complexes with reasonable signal-to-noise. Figures 3.11 and 3.12 show the best-fitting model M5 for the 2000 and 2004 *Chandra* epochs, respectively.

For the 2001, 2013, 2014, 2016, and 2018 *XMM-Newton* epochs, the low spectral resolution of the *pn* and MOS1/2 cameras results in geometrical degeneracies with the `shellblur` model, and thus we fix all of the geometrical parameters except the velocity expansion and the column density of the ejecta core in component C1 (since the spectral resolution of *XMM-Newton* at >4 keV is sufficient to estimate the width of Fe-K line). In this manner, we obtain and constrain the temperature, absorption, high temperature velocity expansion and abundance parameters for model M5 for these epochs.

We highlight an interesting feature at ~ 7.3 – 7.6 keV in the 2000 epoch spectrum (see

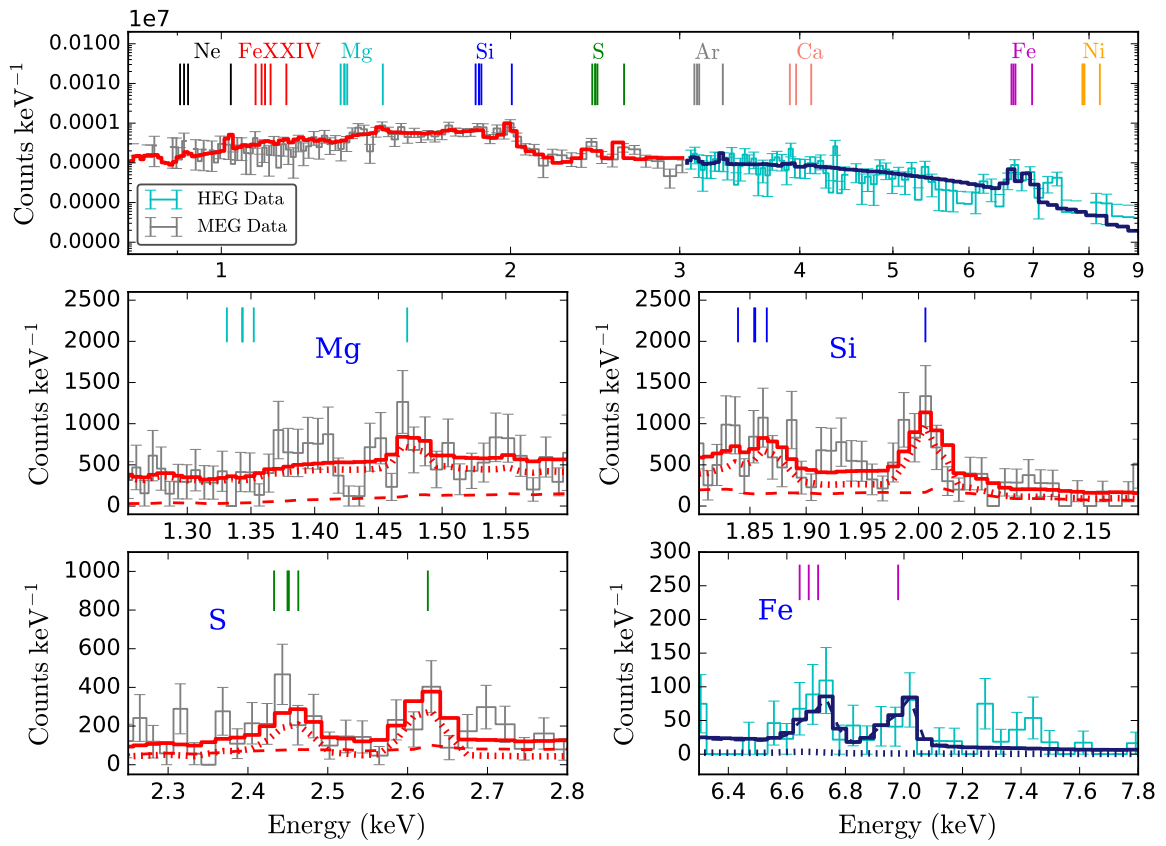


Figure 3.11: Same as Fig. 3.9 but for the 2000 epoch *CXO* HEG/MEG spectra.

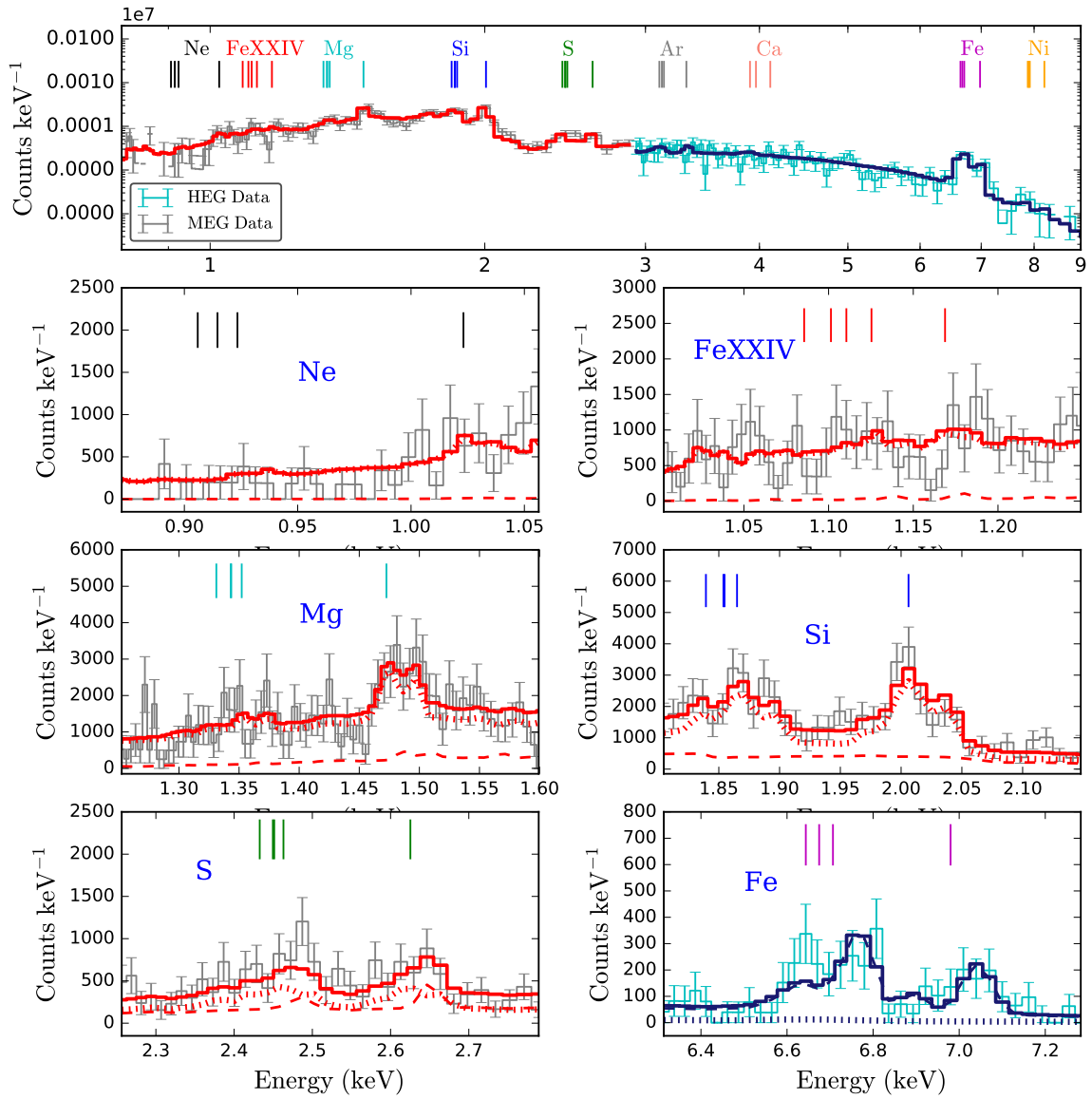


Figure 3.12: Same as Fig. 3.9 but for the 2004 epoch *CXO* HEG/MEG spectra.

Fig. 3.11) that the M5 model fails to fit. This feature is comprised of 11 counts, well above the expected continuum signal and unexpected given Chandra's strongly decreasing effective area here. We verified that the emission at ~ 7.4 keV in the 2000 epoch does not come from contamination of other sources (AGN or off-nuclear point-sources) in the HETG dispersed spectra. The feature does not obviously correspond to any previously modeled element (e.g., H-like or He-like Fe, as indicated in Fig. 3.11 or Ni XXVII and XXVIII at ~ 7.8 keV and 8.1 keV, respectively). We see no similar velocity components from other elements.

We consider briefly that this line complex arises from possible He-like and/or H-like Fe emission associated with "bullet"-like Fe ejecta (e.g., similar to Cas A Willingale et al. 2002), and model it with a third NEI plasma component convolved with a highly polar ($\theta_{min} \sim 85^\circ$) geometry and an exceptionally high expansion velocity ($v_{max} \sim 23000$ km s $^{-1}$). The result provides a reasonable match to the data, as seen in Fig. 3.13. The C-stat value for the epoch 2000 modestly improves by $\Delta C\text{-value}=2.13$ compared to the nominal M5 model. This Fe complex also appears weakly as a residual in the 2001 spectrum, but not in the following epochs. For the 2001 epoch, adding such a "bullet"-like Fe plasma structure improves significantly the fit to the *pn* data at ~ 7.4 keV (see Figure A.1). Alternatively, the line could be associated with a highly redshifted Ni XXVII (~ 7.8 keV) or XXVIII (8.1 keV) "bullet"-like structure ($v_{max} \sim 15000\text{--}26000$ km s $^{-1}$, $i=90^\circ$). We do not consider this possibility as viable as Fe, however, because the flux of this component would be roughly equal to what we estimate for all of the lower velocity Ni, even before we correct for any potentially high N_{ejecta} , as found for Fe. Finally, another possible identification could be the 7.47 keV Ni $K\alpha$ fluorescent line, but this would be quite unexpected as it requires cold reflection (e.g., Yaqoob & Murphy 2011) and we do not see the correspondingly stronger 6.4 keV Fe $K\alpha$ in the 2000 epoch spectra.

We also find mild discrepancies between the model and the He-like S and Fe data line shapes in the 2004 epoch spectrum (Fig. 3.12). We do not attempt further fine-tuning, as the differences do not appear internally consistent. That is, the bright unmodeled peaks

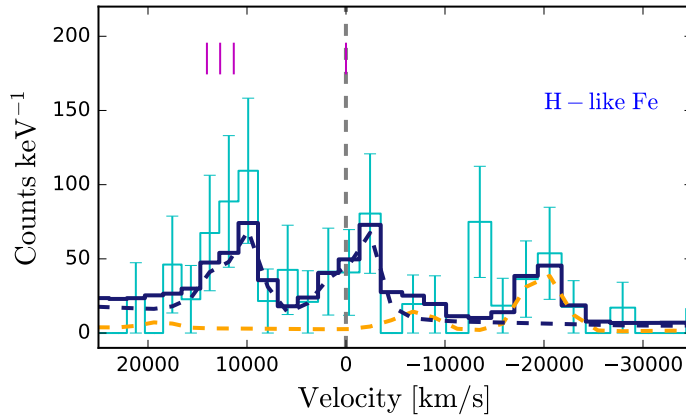


Figure 3.13: The Fe emission complex of the 2000 epoch HEG-*Chandra* data (cyan histogram), centered on the H-like line in velocity space (vertical grey dashed line). In addition to the hotter C1 component (dashed blue curve) obtained from model M5, we show a possible third NEI plasma component with a shell expansion velocity of ~ 23000 km/s; the total model is shown as the black histogram. The magenta vertical lines denote the location in velocity space of the H-like and He-like Fe lines.

in the He-like S or Fe lines do not occur in the same portion of the velocity profile. We simply note that abundance inhomogeneities and asymmetries may exist.

In Figures 4.2–4.4, we can see how various parameters evolve with time, since the explosion of the SNe; we adopt an explosion date of 1995.4. The grey region is the apparent time during which the SNe forward shock interacted with a dense shell, based on 1-D hydro-dynamical simulations (D10). Table 3.2 gives the errors from M5 for the 2000, 2001, 2004, 2009, 2013, 2014, 2016 and 2018 epochs, while Table 4.1 shows the abundances obtained in these epochs. In the next section, we search for plausible physical explanations for model M5 and its parameter evolution, and try to discuss the CSM geometry of SN 1996cr.

Table 3.2: Spectral parameters for model M5 at different epochs. *Col. 1:* Epoch of combined X-ray observations. *Col. 2:* satellite and instrument. *Column 3:* spectral model component. *Col. 4:* column density N_{H} in units of $\times 10^{22} \text{ cm}^{-2}$. *Col. 5:* temperature in keV. *Col. 6:* opening-angle measure in degrees ($^{\circ}$). *Col. 7:* inclination angle respect to the line-of-sight in degrees ($^{\circ}$). *Col. 8:* column density N_{ejecta} of ejecta interior to reverse shock in units of $\times 10^{22} \text{ cm}^{-2}$. *Col. 9* unabsorbed $0.5\text{--}10.0 \text{ keV}$ flux in units of $\times 10^{-12} \text{ erg cm}^{-2} \text{ s}^{-1}$. Upper limits are defined with $3\text{-}\sigma$ confidence level.

Epoch	Telescope	Model	N_{H}	kT	θ_{min}	i	γ_{max}	N_{ejecta}	Unabs. Flux
2000	<i>Chandra</i> -HETG	TBabs $_{C1}$ (shellblur $_{C1}$ *vpshock $_{C1}$) +	$2.3^{+0.8}_{-0.6}$	$12.9^{+5.5}_{-3.2}$	$< 70^{\circ}.0$	$55^{\circ}.0(\text{fix})$	$3618.3^{+410.3}_{-1279.3}$	$63.8^{+97.1}_{-43.5}$	$2.2^{+0.2}_{-0.2}$
		TBabs $_{C2}$ (shellblur $_{C2}$ *vpshock $_{C2}$)	$0.13^{+0.1}_{-0.1}$	$2.3^{+0.7}_{-0.4}$	$33^{\circ}.0^{+9.4}_{-10.8}$	$55^{\circ}.0(\text{fix})$	$3619.2^{+482.6}_{-288.9}$	$0.96^{+1.3}_{-0.7}$	$0.6^{+0.1}_{-0.1}$
2001	<i>XMM-Newton</i>	TBabs $_{C1}$ (shellblur $_{C1}$ *vpshock $_{C1}$) +	$2.0^{+0.9}_{-0.5}$	$16.3^{+2.6}_{-2.2}$	$64^{\circ}.1^{+5.1}_{-6.7}$	$55^{\circ}.0(\text{fix})$	$5717.3^{+760.7}_{-878.8}$	$74.9^{+23.9}_{-18.1}$	$1.6^{+0.1}_{-0.1}$
		TBabs $_{C2}$ (shellblur $_{C2}$ *vpshock $_{C2}$)	$1.1^{+0.1}_{-0.1}$	$3.2^{+0.3}_{-0.3}$	$< 54^{\circ}.0$	$55^{\circ}.0(\text{fix})$	$4780.0^{+1633.6}_{-1778.8}$	$1.8^{+2.2}_{-1.8}$	$1.5^{+0.1}_{-0.1}$
2004	<i>Chandra</i> -HETG	TBabs $_{C1}$ (shellblur $_{C1}$ *vpshock $_{C1}$) +	$1.9^{+0.4}_{-0.3}$	$10.3^{+1.6}_{-1.4}$	$54^{\circ}.9^{+7.3}_{-10.1}$	$55^{\circ}.0(\text{fix})$	$6232.8^{+884.5}_{-733.7}$	$76.1^{+43.4}_{-28.4}$	$3.4^{+0.2}_{-0.2}$
		TBabs $_{C2}$ (shellblur $_{C2}$ *vpshock $_{C2}$)	$0.2^{+0.1}_{-0.1}$	$2.5^{+0.5}_{-0.4}$	$33^{\circ}.5^{+11.0}_{-11.8}$	$55^{\circ}.0(\text{fix})$	$6333.2^{+415.2}_{-203.9}$	$2.3^{+1.1}_{-0.8}$	$1.1^{+0.1}_{-0.1}$
2009	<i>Chandra</i> -HETG	TBabs $_{C1}$ (shellblur $_{C1}$ *vpshock $_{C1}$) +	$2.5^{+0.4}_{-0.3}$	$33.5^{+25.3}_{-12.1}$	$70^{\circ}.0^{+5.1}_{-5.1}$	$55^{\circ}.0(\text{fix})$	$3085.9^{+353.7}_{-160.6}$	$59.5^{+13.9}_{-11.6}$	$2.9^{+0.1}_{-0.1}$
		TBabs $_{C2}$ (shellblur $_{C2}$ *vpshock $_{C2}$)	$0.2^{+0.03}_{-0.03}$	$2.8^{+0.2}_{-0.1}$	$32^{\circ}.3^{+3.7}_{-3.6}$	$55^{\circ}.0(\text{fix})$	$4522.1^{+166.7}_{-108.1}$	$2.0^{+0.4}_{-0.3}$	$1.6^{+0.02}_{-0.03}$
2013	<i>XMM-Newton</i>	TBabs $_{C1}$ (shellblur $_{C1}$ *vpshock $_{C1}$) +	$0.8^{+0.1}_{-0.1}$	$10.0^{+0.9}_{-0.7}$	$< 69^{\circ}.7$	$55^{\circ}.0(\text{fix})$	$4777.0^{+636.4}_{-1174.0}$	$29.2^{+21.2}_{-12.2}$	$1.6^{+0.1}_{-0.1}$
		TBabs $_{C2}$ (shellblur $_{C2}$ *vpshock $_{C2}$)	$0.7^{+0.1}_{-0.1}$	$2.1^{+0.3}_{-0.2}$	$30^{\circ}.0(\text{fix})$	$55^{\circ}.0(\text{fix})$	$4500.0(\text{fix})$	$2.0(\text{fix})$	$0.6^{+0.04}_{-0.04}$
2014	<i>XMM-Newton</i>	TBabs $_{C1}$ (shellblur $_{C1}$ *vpshock $_{C1}$) +	$0.9^{+0.4}_{-0.2}$	$10.4^{+1.6}_{-1.1}$	$70^{\circ}.0(\text{fix})$	$55^{\circ}.0(\text{fix})$	$3546.5^{+783.7}_{-1321.4}$	$9.5^{+12.2}_{-5.0}$	$1.1^{+0.1}_{-0.1}$
		TBabs $_{C2}$ (shellblur $_{C2}$ *vpshock $_{C2}$)	$0.5^{+0.1}_{-0.1}$	$2.1^{+0.3}_{-0.2}$	$30^{\circ}.0(\text{fix})$	$55^{\circ}.0(\text{fix})$	$4500.0(\text{fix})$	$2.0(\text{fix})$	$0.5^{+0.04}_{-0.04}$
2016	<i>XMM-Newton</i>	TBabs $_{C1}$ (shellblur $_{C1}$ *vpshock $_{C1}$) +	$0.8^{+0.2}_{-0.1}$	$8.6^{+1.1}_{-1.0}$	$70^{\circ}.0(\text{fix})$	$55^{\circ}.0(\text{fix})$	$4602.4^{+1721.5}_{-1502.5}$	$24.0^{+22.0}_{-11.8}$	$1.2^{+0.1}_{-0.1}$
		TBabs $_{C2}$ (shellblur $_{C2}$ *vpshock $_{C2}$)	$0.7^{+0.2}_{-0.2}$	$1.4^{+0.3}_{-0.2}$	$30^{\circ}.0(\text{fix})$	$55^{\circ}.0(\text{fix})$	$4500.0(\text{fix})$	$2.0(\text{fix})$	$0.8^{+0.1}_{-0.1}$
2018	<i>XMM-Newton</i>	TBabs $_{C1}$ (shellblur $_{C1}$ *vpshock $_{C1}$) +	$0.73^{+0.1}_{-0.1}$	$8.6^{+1.6}_{-1.2}$	$70^{\circ}.0(\text{fix})$	$55^{\circ}.0(\text{fix})$	$4781.3^{+1045.3}_{-1180.8}$	$51.3^{+41.1}_{-28.6}$	$0.8^{+0.1}_{-0.1}$
		TBabs $_{C2}$ (shellblur $_{C2}$ *vpshock $_{C2}$)	$0.7^{+0.1}_{-0.1}$	$2.7^{+0.5}_{-0.5}$	$30^{\circ}.0(\text{fix})$	$55^{\circ}.0(\text{fix})$	$4500.0(\text{fix})$	$2.0(\text{fix})$	$0.5^{+0.1}_{-0.1}$

Chapter 4

Results and discussion

In §3, we derived a best-fit model to match the 2009 epoch X-ray spectra of SN 1996cr and extended it to other epochs spanning ± 9 years. The spectra are successfully explained with only two distinct NEI components: a hot, heavily absorbed, high-latitude polar shock (C1) and a cooler, moderately absorbed, wider polar shock (C2). Here we explore the physical nature of each component and how the parameters evolve over time.

4.1 Interpretation of Model M5 at 2009 epoch

The shock interaction in SNe can be quite complex (Chevalier et al. 1992; Michael et al. 2002), since it depends on the 3-D density distributions of the expanding ejecta and pre-existing CSM (e.g. DeLaney et al. 2010; Milisavljevic & Fesen 2013; Orlando et al. 2015; Orlando et al. 2016). The canonical self-similar description of a spherically symmetric shock traveling into a spherically symmetric power-law medium produces a double-shock structure, consisting of a blast wave (forward shock) that travels outwards into the CSM and a reverse shock that travels back (in a Lagrangian sense) into the SN ejecta (Chevalier 1982b). Between the forward and reverse shocks, there should exist shocked CSM and ejecta material separated by a contact discontinuity. Shock expansion typically results in X-ray and radio emission associated with the two shocks (Chevalier

1982a), with the forward/reverse shocks thought to dominate at hard/soft X-rays energies ($\gtrsim 2$ keV / $\lesssim 2$ keV), respectively.

Core-collapse SNe evolve into the wind-driven region created by mass-loss from the progenitor star, and it is this region that subsequently defines the SN expansion, dynamics and kinematics. If the wind parameters remain constant, as is expected for most SNe, then the wind region should have a density profile which goes as $\propto r^{-2}$. In the particular case of SN 1996cr, D10 previously demonstrated that the wind parameters changed hundreds to thousands of years before explosion, resulting in a fast-to-slow wind collision and the formation of a dense shell of swept-up CSM. Thus, SN 1996cr is somewhat different from the canonical picture, due to the nature of the medium surrounding the SN. A comparison between several epochs of X-ray spectra and 1-D hydrodynamical simulations led D10 to propose that SN 1996cr initially exploded into a low-density medium and, after ~ 1.5 yrs, the blast wave encountered a dense shell of material, at ≈ 0.03 pc from the progenitor star. The estimated width and density of this shell was found to be consistent with expectations from a WR or BSG wind having swept up a previously existing RSG wind. In this model, the bulk of the X-ray emission for the first 7 years arose from the forward shock, while the reverse shock emission was dominant thereafter. The D10 model offered up a successful physical framework that fit the continuum shapes and emission line strengths reasonably well, although that work made no attempt to model the line profiles (shape or velocity) as we have done here. Of particular importance, D10 assumed spherical symmetry and found that the observed temperature stratification, as evidenced by the flat continuum and line strengths of the SN 1996cr spectra, could be naturally explained as the sum of the different radial components of the shock. Dewey et al. (2011) built upon the 1-D model of D10 using a 3-D convolution technique (based on Dewey & Noble 2009) to fit the velocity profiles. Dewey et al. (2011) principally reported on an analysis of the Si and Fe lines profiles for the 2009 epoch, which implied a non-spherical ejecta–CSM interaction geometry, but did not investigate the evolution as we do here.

From our analysis of the emission line shapes in §3.1.2, we are able to reject a spherically

symmetric 4π emission geometry at high confidence. We can likewise reject a ring-like emission geometry (e.g., similar to SN 1987 Michael et al. 2002; Zhekov et al. 2006; Dewey et al. 2008) with high confidence. Instead, we find that the S, Si, and Mg lines are best-fit by an inclined, wide-angle polar geometry (C2) covering $\approx 2\pi$ solid angle on the sky, while the highest ionization Fe XXVI line is best fit by a similarly inclined narrow-angle polar geometry. Intriguingly, the more modest ionization Fe XXIV and XXV lines have best-fit values intermediate between the wide and narrow components, suggesting potential contributions from both, although the uncertainties that remain are large. Substantial degeneracy appears to remain between the opening and inclination angles for the narrow-angle component, as seen in Fig. 3.7. However, it is reassuring that the best-fit inclination angle for both the C1 and C2 components appears to be $\sim 55^\circ$.

One novelty of spectral models M2-M6 is that, under the assumption of symmetry, they place constraints on the overall inner ejecta column density, N_{ejecta} . For coding efficiency, we naively modeled this absorption assuming a uniform spherical distribution and solar abundances. The first assumption regarding uniformity should be reasonable; while the ejecta density is very steep initially ($\sim r^{-9}$), after a few years the density profile of the inner ejecta should become relatively flat (see Fig. 3 of D10), although this could differ by factors of at least a few in practice given the polar geometries our models favor. The latter assumption of solar abundances is unlikely to be valid, given the expected ejecta composition, although this should simply lead to degeneracy between the column density and the high-Z abundances (e.g., Kaastra et al. 2008). Nonetheless, we can still try to interpret our results to give some important insights. We found in §3.1.4 that the farside of the C1 velocity profile must be absorbed by a neutral hydrogen column density ejecta of $N_{\text{ejecta}} = 59.5^{+13.9}_{-11.6} \times 10^{22} \text{ cm}^{-2}$, while the C2 velocity profile only requires $2.0^{+0.4}_{-0.3} \times 10^{22} \text{ cm}^{-2}$. Assuming a shock radius of $\sim 0.065 \text{ pc}$ at the 2009 epoch based on the D10 model, these values translate to estimated angle-averaged densities of 1.7×10^6 and $2.6 \times 10^5 \text{ amu cm}^{-3}$, respectively, for an inclination angle of 55° . The latter is in relatively good agreement with the 1-D model of D10 (see their Fig. 3), demonstrating the rough

validity of that model. The former, however, is higher by a factor of ~ 7 , indicating a much higher concentration of high-Z material along this line-of-sight. The large disparity between the N_{ejecta} values, which in theory should probe roughly comparable inner ejecta densities, implies a strongly inhomogeneous ejecta structure, with either substantially denser material behind the narrow-angle C1 component, or drastically higher ionization levels behind component C2.

More complex geometries (e.g., a partial or elliptical ring, clumps) may provide acceptable fits to the line profiles — e.g., emission from two points opposite each other on a ring will be highly degenerate with the narrow-angle polar emission we currently observe — however, we feel that these need substantial further observational or theoretical justification to consider them. Unfortunately, the X-ray observations are unresolved and VLBI observations have not yet managed to define the structure in SN 1996cr (Bietenholz 2014).

Our geometrical constraints do not necessarily invalidate the work of D10, which appear to effectively capture the broad characteristics of the shock interaction and explain several key observational signatures (e.g., the CSM density profile and shock energetics leading to the X-ray light curve, and elemental abundances). We already noted the impressive self-consistency between the D10 inner density and the best-fit $N_{\text{ejecta,C2}}$ for component C2. D10 never incorporated the HETG emission line velocity widths into their model, so it is perhaps not surprising that we find discrepancies by factors of 2–5 between our C1 and C2 component velocities and the forward shock velocity derived by D10 from the 2009 epoch (see panel (a) of Fig. 4.2). Our results are generally consistent with those of Dewey et al. (2011), who incorporated 3-D convolution models with velocity effects to fit the 2009 epoch HETG continuum and emission line spectra. Furthermore, Dewey et al. (2011) found that the temperature-dependent line profiles implied that the progenitor CSM around SN 1996cr was most likely denser at the poles.

Based on our best-fit polar geometry, our results imply that the solid area covered by the shock must be proportionally smaller than 4π by factors of ≈ 2 for component C2 and ≈ 15 –

30 for component C1. For the C2 component, this naively implies only minor adjustments to the CSM density, radius, or ejecta energetics, while for C1, a more substantial adjustment will be required. A more complex issue is how the introduction of two spatially distinct shocks, components C1 and C2, will affect the layered temperature stratification and small-scale clumping introduced in the D10 model, which ultimately contribute to the continuum shape and emission line strengths.

The potential polar geometry of the ejecta-CSM interaction of SN 1996cr could result from either bullet-like ejecta (as in Cas A) or previous mass-loss phases of a massive progenitor. In the case of the former, we might expect higher density ejecta at higher velocities. Regarding the latter, one possibility to sculpt such a CSM feature is from an eccentric binary system undergoing eruptive mass loss. We directly observe similar dense bipolar CSM regions in evolved stars like η Carinae (Davidson & Humphreys 1997; Smith et al. 2007, 2018) and Betelgeuse (Kervella et al. 2018), as well as indirectly in SN imposters like UGC2773-OT and SN 2009ip (e.g., Smith et al. 2010; Mauerhan et al. 2014; Reilly et al. 2017) or type IIin SNe such as SN 2012ab and SN 2015bh (Thöne et al. 2017; Bilinski et al. 2018).

The two distinct shock components here draw some parallels to the two shock components seen in SN 1987A. For example, Dewey et al. (2012) were able to successfully model the X-ray spectra of SN 1987A as the weighted sum of two NEI components from two simple 1-D hydrodynamic simulations: a ≈ 0.5 keV component associated with the interaction of a dense equatorial ring ($\sim 2^\circ$ width) and a $\sim 2\text{--}4$ keV component associated with the interaction of a sparser surrounding HII region ($\sim 30^\circ$ width) producing very-broad emission lines. The shock going into the ring is slower and cooler, while the shock above and below the ring (into less dense material) is faster and hotter. While SN 1996cr does not appear to have an equatorial ring geometry, the concept of two shocks propagating into dense and less dense CSM still may apply. However, our favored interpretation is somewhat different, as we will show later.

Finally, we note that the Fe K-shell line luminosities and energy centroids observed

in nearby supernova remnants (SNRs) have been found to exhibit clear distinctions based on Ia and CC-SNRs progenitor types, explosion energy, ejecta mass, and circumstellar environment (e.g., Yamaguchi et al. 2014; Patnaude et al. 2015). Typically, the Fe K-shell centroid energies from type Ia SNRs have <6.55 keV, implying lower ionization than those from CC-SNRs with ≥ 6.55 keV. SN 1996cr, a CCSN, follows this general scheme, with a centroid energy of $6684.4^{+9.6}_{-7.6}$ eV and total Fe K-shell flux and luminosity of $(2.4 \pm 0.3) \times 10^{-5}$ photons $\text{cm}^{-2} \text{s}^{-1}$ and $(3.9 \pm 0.5) \times 10^{46}$ photons s^{-1} for the 2009 epoch, respectively. As such, SN 1996cr lies in the extreme upper right corner of the “Yamaguchi plot” (see Figure 1 of Yamaguchi et al. 2014), implying that Fe-rich ejecta reach the shock interaction region relatively quickly during the explosion. Notably, SN 1996cr’s values lie well outside of the theoretical models. While beyond the scope of the current work, it could be interesting to explore the theoretical and practical implications of extreme sources like SN 1996cr in the Yamaguchi plot.

4.2 Time Evolution of Parameters

Following on from our interpretation of the 2009 epoch, we investigate the evolution of the spectral parameters with time in Figures 4.1–4.4.

Taking cues from D10, we tentatively identify component C2 with the forward shocked CSM and the component C1 with a (focused) reverse and/or reflected shocked ejecta. A key issue to reconcile, however, is why we observe distinct velocity profiles. One possible origin for this difference could be due to asymmetric ejecta from the onset of the explosion, e.g., as has been argued for SN 1987A (Larsson et al. 2016). Another possibility is that the CSM is asymmetric, as is expected around many stars which have aspherical, often bipolar or toroidal structures surrounding them (van Marle et al. 2010). The latter, particularly if it affected the wind-blown shell, might lead to an asymmetric or focused reflected shock. Even if the explosion began with spherically symmetric ejecta, realistic multi-dimensional simulations suggest that relatively small instabilities or variations within the CSM or

the wind-blown shell (e.g., Dwarkadas 2008) could lead to wrinkled or corrugated SN shocks (Dwarkadas 2007b). The interaction of such a shock wave with even a spherical circumstellar shell will occur at somewhat different times along the length of the shell, resulting in a potentially asymmetric reverse shock. Moreover, if the circumstellar shell was oblate, then the expanding shock wave could have impacted one portion of the shell before another, and led to a reflected shock which was highly enhanced and perhaps even focused onto a small portion of the ejecta. In summary, we should not be too surprised to see aspherical reflected shocks (Dwarkadas 2007b) as a result of any combination of these effects. Given the higher density of the ejecta, we might expect the reflected shock to dominate the overall emission at late times.

We begin by commenting on the evolution of the two foreground column density terms in model M5, shown in panel (a) of Figure 4.1. The nominal Galactic absorption (*dashed black line*) should set a lower bound on the expected absorption. The fact that component C2 is best-fit with values consistent with the Galactic N_{H} in epochs 2000, 2004, and 2009 implies that there is little host obscuration along the line of sight, such that any excess absorption should be related to changes in the CSM of the SN. One important consideration, however, is the potential influence that the known energy-dependent cross-calibration offsets between *XMM* and *Chandra* may have on our best-fit parameters. In particular, the *XMM pn* detector is known to find $\sim 10\text{--}20\%$ cooler temperatures or softer photon indices compared to *Chandra*'s ACIS detector for identical objects (e.g., Nevalainen et al. 2010; Madsen et al. 2017). Given fitting degeneracies between temperature and column density, we might expect to observe modest offsets between either the best-fit N_{H} or kT values from *Chandra* and *XMM-Newton* spectra, in the sense that *XMM-Newton* may yield somewhat lower temperatures or higher column densities. Thus the mildly higher column densities we find for the *XMM-Newton* epochs compared to the *Chandra* ones could be due to this effect. Although we cannot rule out that some portion of the obscuration is intrinsic to SN 1996cr, to be conservative, we consider best-fit values of $\lesssim 7 \times 10^{21} \text{ cm}^{-2}$ for *Chandra* and *XMM-Newton* to indicate Galactic-only (no CSM) obscuration.

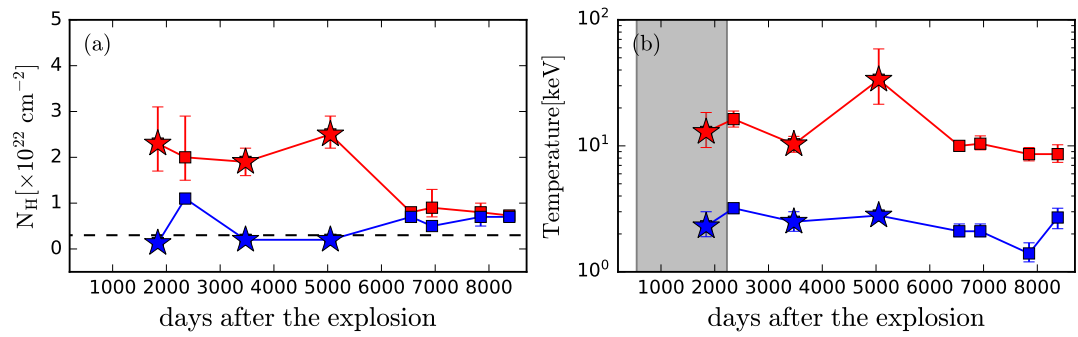


Figure 4.1: Evolution of parameters in different epochs. *Red symbols* and *blue symbols* denote parameters associated with the C1 (high kT , high N_{H} , narrow polar angle) and C2 (low kT , low N_{H} , wider polar angle) components, respectively. *Open symbols* denote parameters that were fixed to previous best-fit values in the fitting analysis. The *gray region* in each panel denotes the epoch during which the forward shock interacted with the dense CSM shell, according to the model of D10. *Stars* and *squares* represent *Chandra* and *XMM-Newton* data, respectively. Panels (a) and (b) show the foreground absorption (N_{H}) and NEI temperatures of components C1 and C2. The *dashed black line* in panel (a) represents the estimated Galactic column density ($3 \times 10^{21} \text{ cm}^{-2}$); values significantly above this imply extra internal absorption either from the disk of the Circinus Galaxy or the immediate vicinity of SN 1996cr (Bauer et al. 2008).

With this in mind, component C2 appears to be relatively unabsorbed at all times, except perhaps around ≈ 2300 days where we find a value of $\approx 1.1 \times 10^{22} \text{ cm}^{-2}$. This brief enhancement could be due to obscuration associated with either clumpy unshocked CSM (linked to the evolution of the progenitor) or the compression of shocked CSM and ejecta material in the immediate vicinity of the forward and reverse shocks. In the model of D10, the column density of the shocked CSM behind the forward shock reaches a maximum of $5 \times 10^{21} \text{ cm}^{-2}$ around day ~ 2400 , since at this time the forward shock interacts with the high density outer edge of material swept up by the Wolf-Rayet wind. This value is consistent with that measured ($\sim 4 \times 10^{21} \text{ cm}^{-2}$) considering also a Galactic absorption of $7 \times 10^{21} \text{ cm}^{-2}$.

On the other hand, component C1 is best-fit by a high, roughly constant N_{H} of $\approx (2-2.5) \times 10^{22} \text{ cm}^{-2}$ at early times ($\approx 1700-5500$ days). The strong difference between the early C1 and C2 column densities implies that either: (i) there are strong, dense asymmetries in the foreground (unshocked) CSM that somehow obscure the C1 emission more than C2 (e.g., SN 2005kd, SN 2006jd, and SN 2010jl; Katsuda et al. 2016); (ii) the components are radially offset such that the C1 emission must pass through the dense shocked material (e.g. the dense shell) swept up by the C2 shock; (iii) the absorption arises from dense clumps in close proximity to or likely embedded within the C1 shock itself; or (iv) strong differences in the degree of ionization exist along the line-of-sight of the C2 component, augmenting the apparent absorption.

If C1 is indeed associated with the shocked ejecta, then this moderate absorption value can be explained as being viewed through the dense shell at early times. At later times the effect of the dense shell should diminish, potentially explaining the drop to $N_{\text{H}} \approx (7-9) \times 10^{21} \text{ cm}^{-2}$, only slightly above the Galactic value. This would be consistent with the reverse/reflected shock interpretation for the C1 component. In the D10 simulations, the shock-shell interaction is complete by ~ 7 years. In a doubling time or so, all knowledge of the shell is lost (see also Dwarkadas 2005), as the shell structure has been obliterated. This implies that at late times there will be little extra density structure between the forward

and reverse/reflected shocked material, with the difference arising primarily from newly shocked CSM, which should have a relatively low column.

We note that the type IIIn SNe 2010jl and 2005ip show a similar tendency. For instance, the column density from SN 2010jl was initially found to have $N_{\text{H}} > 10^{24} \text{ cm}^{-2}$ and was seen to decrease by two orders of magnitude in the first ~ 1000 days (Chandra et al. 2015; Chandra 2018), while SN 2005ip was initially found to have $N_{\text{H}} \approx 5 \times 10^{22} \text{ cm}^{-2}$ and dropped by one order of magnitude (Katsuda et al. 2014).

Next, we look at the evolution of the two electron temperature components in model M5, shown in panel (b) of Figure 4.1. Both components remain distinctly separated and exhibit marginal rises between days ~ 1700 – 2200 followed by mild overall declines between days ~ 2200 – 8000 . There is an uptick in the temperature around day ~ 5000 for component C1, and around day ~ 8500 for component C2, but these are not significant after factoring in the errors. Unfortunately, the temperature of component C1 is somewhat difficult to constrain, particularly when coupled with high N_{H} values, because neither *Chandra* nor *XMM-Newton* has good sensitivity above ~ 7 – 8 keV (e.g., Chandra 2018), while *NuSTAR* imaging suffers from strong AGN contamination (Arévalo et al. 2014).

It is important to stress, as in D10, that at least two temperatures are required in order to fit both the relatively flat continuum and the numerous emission lines, which span a large range in excitation energy. We initially equate these temperatures with the postshock temperatures behind the forward and reverse shocks, respectively. The temperatures essentially depend on the square of the velocity and the mean molecular weight as $T_{\text{s}} = 3\mu m_{\text{H}} v_{\text{s}}^2 / 16k$. From Fig. 4.2 in panel (a), we see that the velocities of C1 and C2 are comparable at all times, implying that a difference in mean molecular weights drives much of the temperature difference. Thus, the shocked ejecta (C1) has a much higher mean molecular weight than the shocked CSM (C2). This is probably reasonable, since we expect the ejecta to contain a higher proportion of heavy elements. If the progenitor was a Wolf-Rayet star, containing no H and maybe no He, then the ejecta proportion of heavy elements would be considerably higher. This is also visible in Fig. 4.4 panel (a), where

the Fe abundance of the components is shown to be much higher than solar.

The evolution of the shell expansion velocity for the two components of model M5 is shown in panel (a) of Figure 4.2. The velocities of both components are found to increase from relatively low values of $\sim 3500 \text{ km s}^{-1}$ to maxima of $\sim 6000 \text{ km s}^{-1}$ between days ~ 1700 – 3500 , roughly coinciding with the epoch during which the forward shock is thought to exit the swept-up shell bordering the wind-blown bubble in the D10 model (denoted by the *grey block* in Figures 4.1–4.4). For comparison, we show the evolution of the forward and reverse/reflected shock velocities obtained in D10 (dashed *black* and *green* lines, respectively). In D10, following the SN explosion, the forward shock expanded rapidly ($\sim 10^4 \text{ km s}^{-1}$) until it encountered the dense shell of material, which led to a drastic drop in the forward shock velocity to $\sim 2500 \text{ km s}^{-1}$ at day ~ 800 . Between days ~ 500 – 1500 , the region between the forward and reverse shocks became highly compressed; after exiting the shell, the forward shock expanded into a lower density wind region and its velocity increased again (due to pressure differential). By contrast, the reverse shock velocity between days ~ 800 – 1000 increased sharply to a value of $\sim 10^4 \text{ km s}^{-1}$. This sharp increase arises from the contribution of the reflected shock (created by the interaction of the ejecta with the high-density shell) that travels rapidly back into the ejecta. Beyond day ~ 1000 , the reverse shock velocity decreases as the reverse shock expands into the steep density incline and sweeps up more material. Intriguingly, the observational data for both components C1 and C2 appear more consistent with the forward shock model than the reverse shock over this time frame.

The expansion velocities of both C1 and C2 decrease substantially between days ~ 3500 – 5000 , which is not predicted by the forward shock model [dashed *black* line in panel (a) of Fig. 4.2]. This discrepancy, however, is not that surprising given the lack of late-time data as input to the D10 model. For instance, D10 had to assume values for the radius and thickness of the shell, as well as the CSM density beyond it. Minor modifications, such as moving the shell inward, modifying its thickness, and modifying the outer CSM density, could potentially account for the velocity difference and evolution. Unfortunately, beyond

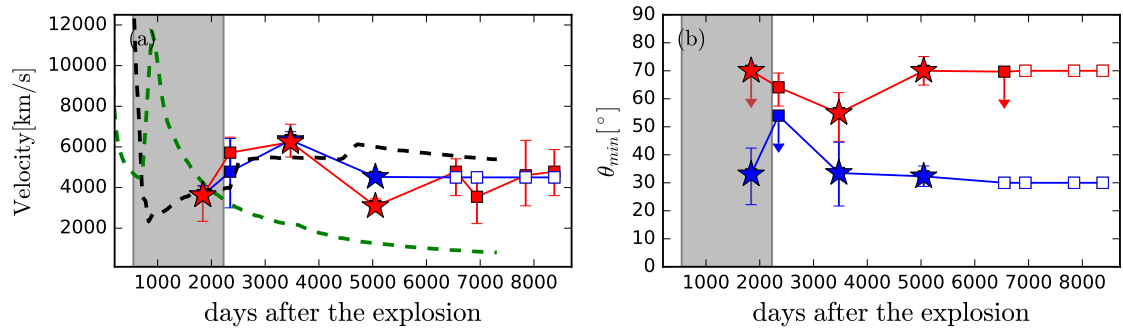


Figure 4.2: Same as Fig. 4.1 but panels (a) and (b) show the geometrical model velocity expansion and opening angle, respectively. The *dashed black* and *green* lines in panel (a) represents the forward and reverse velocities obtained by D10

day 5000 our velocity constraints remain rather limited due to the crude CCD-resolution of the *XMM-Newton pn* camera. To within the uncertainties, component C1 remains roughly constant or mildly increases between days ~ 5000 – 9000 , while component C2 cannot be well-constrained and therefore was fixed to its value at day ~ 5000 . The roughly constant behavior at late times may support the prediction of D10 that the more recent emission arises from the interaction of the forward shock with a steady wind, in which case the velocity changes very slowly with time. The lower velocities we find from day ~ 5000 onward compared to the D10 predictions may be a consequence of a somewhat higher CSM density, as mentioned already in §4.1. One possibility for the observed data and model mismatch after day ~ 5000 could be because the 1-D simulations do not capture the effects of the 2-D or 3-D asymmetries resulting from either turbulence, asymmetries and inhomogeneities within the progenitor star wind or from instabilities of the ejecta–CSM interaction itself. Considering for the moment various higher dimensionality SNe simulations (e.g. Chevalier et al. 1992; Dwarkadas 2007a; Freyer et al. 2006; van Marle & Keppens 2012; Orlando et al. 2015), we see that asymmetries can lead to complex velocity flows, and rapidly destroy the spherical symmetry of the explosion, if it ever existed.

Panel (b) of Figure 4.2 examines the change in the opening-angles of both components of model M5. We find that, at least when they can be constrained, they do not change dras-

tically with time. Thus the bi-polar geometrical interaction remains relatively unchanged during our observations. This provides some justification for fixing the inclination-angle to 55° , as discussed in §3.1.3. Due to the low spectral resolution of *XMM-Newton*, we only obtain upper limits on the opening-angles for the 2001 and 2013 epochs, and fixed the opening-angles of the C1 and C2 components to previous values of $\sim 70^\circ$ and $\sim 30^\circ$ for epochs 2014–2018, respectively. Furthermore, the C1 opening-angle was initialized with a value of 75° to help the fit-process to converge to a global minimum and prevent the best-fit from settling at the C2 value (e.g., Arnaud et al. 2011). This aspherical interaction is likely a product of the CSM into which the shock is expanding, which formed over various stellar evolutionary phases from Main Sequence (MS) to RSG to Wolf-Rayet (Dwarkadas 2007b; Garcia-Segura et al. 1996; Freyer et al. 2006), for instance. In fact simulations show that the impact of the progenitor mass-loss and velocity wind distribution prior to the SNe can play a critical role in the dynamical evolution of the ejecta-CSM interaction (Dwarkadas 2005, 2007b; Freyer et al. 2006; van Marle et al. 2010; van Marle & Keppens 2012; Dwarkadas & Rosenberg 2013; Patnaude et al. 2017) and in the symmetry of the emission/interaction region. Dwarkadas (2007a) and Freyer et al. (2006) showed that the strong ejecta-CSM asymmetries arise from asymmetries in the progenitor wind even when a spherical explosion is considered. We cannot rule out the possibility that the explosion had an intrinsic asymmetry or was impacted by a binary companion (e.g., SN 1979C, SN 1987A, SN 1993J, SN 2011dh; McCray 1993; Sugerman et al. 2005; Montes et al. 2000; Maund et al. 2004; Folatelli et al. 2014), either of which could affect the resulting symmetry of the ejecta–CSM interaction. For the binary companion case, the expectation is that the winds of the two stars combine to form an aspherical CSM bubble (van Marle et al. 2012). The ejecta itself may be intrinsically asymmetric. In the case of SN 1987A, considering the Doppler shift of the freely expanding ejecta, Larsson et al. (2016) found a clearly asymmetric north-south ejecta distribution. Alternatively, for Cassiopeia A, the spatial distribution of radioactive ^{44}Ti , which probes the explosion asymmetries of CCSNe (e.g., Magkotsios et al. 2010), implies a highly asymmetric bipolar explosion resulting

from a fast-rotating progenitor star (Grefenstette et al. 2014).

Under the assumption that the shock maintains some geometric (reflected) symmetry which is modified by internal obscuration, we show the evolution of the column density of obscuring ejecta (N_{ejecta}) inside the expanding shell in panel (a) of Figure 4.3. If the ejecta and shock regions are expanding more or less symmetrically, this quantity should not evolve strongly.

We find that the ejecta column density associated with component C1 is quite high at all times [$\approx(1-8)\times 10^{23} \text{ cm}^{-2}$], and shows some evidence for a mild (factor of $\sim 2-4$) drop around days 6500–7500. The column density associated with component C2 is generally a factor of $\sim 5-40$ lower [$\approx(1-2)\times 10^{22} \text{ cm}^{-2}$], and is consistent within errors with being constant in time. As we argued already in §4.1, the large disparity between the N_{ejecta} values argues for a strongly inhomogeneous ejecta structure, such that substantially denser and high-Z material lies along the line-of-sight, and therefore likely in the immediate vicinity, of the narrow-angle C1 component.

Additionally, with values of N_{ejecta} in hand and some indication of the shock geometry and evolution from the D10 model, we can estimate the ejecta mass. For the moment, we will assume a spherical uniform distribution for the ejecta, recalling from the 1-D simulation of D10 that the unshocked ejecta density was uniform after ≈ 10 years and from the 2-D simulations of Dwarkadas (2007a), van Marle et al. (2010) and van Marle et al. (2012) that the asphericity of the ejecta-CSM interaction arose from the inhomogeneous CSM, even though the explosion itself was spherically symmetric. We further consider that (i) the C2 shock geometry covers $\approx 2\pi$ solid angle and reproduces all emission lines except FeXXV–FeXXVI, and (ii) the denser material from C1 lies only along the line-of-sight and does not affect our estimate. Thus, using the C2 ejecta density obtained in §4.1 for 2009 and the associated shock radius from D10, we estimate the average ejecta mass as $M_{\text{ejecta}} \sim 6.9 M_{\odot}$. For 2004, we obtained a similar ejecta mass estimate of $M_{\text{ejecta}} \sim 5.3 M_{\odot}$. These outcomes are in reasonable agreement with the ejecta mass quoted by D10, based on hydrodynamical simulations of $M_{\text{ejecta}}=4.5 M_{\odot}$.

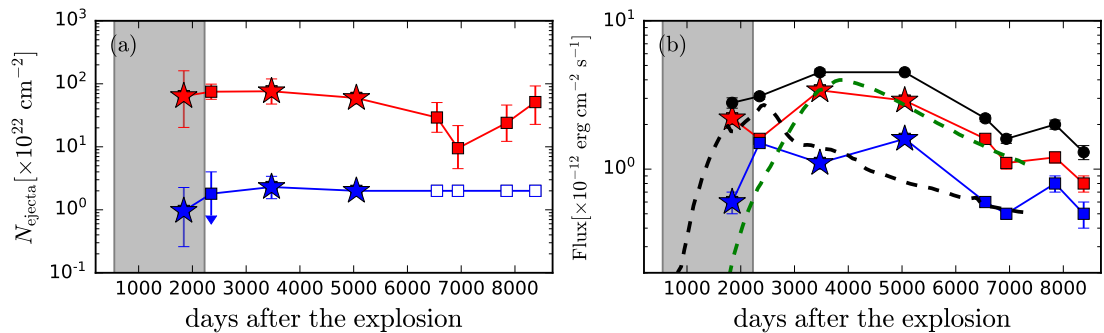


Figure 4.3: Same as Fig. 4.1 but panels (a) and (b) show the geometrical model absorption from inner ejecta and the flux from each component separately and the total flux (*black stars*), respectively.

Panel (b) of Figure 4.3 shows the evolution of the unabsorbed flux for the individual model M5 components C1 (*red symbols*) and C2 (*blue symbols*), as well as the combination (*black circles*), obtained using the XSPEC convolution model `cflux`, as well as the individual contribution to the total flux from the shocked ejecta (*green dashed line*) and CSM (*black dashed line*) computed by D10. This equivalence between the fluxes derived from this method and those calculated from the forward and reverse shock components in D10 is what primarily led to our identification of the two X-ray components as such. The more heavily obscured C1 component has dominated the total flux at all times, comprising between $\approx 54\text{--}76\%$ of the emission at various stages. The total flux reaches a broad maximum between days $\sim 3400\text{--}5000$ (epochs 2004–2009), while individual components C1 and C2 reach maxima around days ~ 3400 and ~ 5000 , respectively. The flux in both components appears to be declining at late epochs, although we note that near day ~ 7000 both show mild upticks. This behaviour could be due to many things such as changes in temperature, ionization, or a change in wind velocity (e.g., episodic RSG mass loss rates prior to the explosion). We note that the late-time fluxes of components C1 and C2 show reasonable agreement with the model shocked ejecta and CSM fluxes from D10, respectively, while at early times the assignment appears reversed (i.e., C1 matches the model CSM flux better, and C2 matches the model ejecta flux better).¹

¹This lack of inversion may be rooted in the implicit assumption the NEI plasma model makes about

Finally, in panels (a) and (b) of Figure 4.4 we track the evolution of the elemental abundances of Fe and Si, respectively. In Table 4.1 we show the abundance values for all constrained elements with $Z \geq 10$ obtained with model M5, for both components, at different epochs. Due to the heavily obscured nature of component C1, we are only able to obtain tight constraints on the Fe abundance. Additionally, elements such as Ne, Ar and Ca show only weak emission lines, and thus are difficult to constrain in general. We find that the Fe abundance for C1 is “super-solar” ($\sim 2 Z_{\text{Fe},\odot}$) at day ~ 1700 and increases smoothly to $\sim 6 Z_{\text{Fe},\odot}$ over the span of ~ 7000 days. This may suggest that we are gradually looking deeper into the ejecta with time. On the other hand, we find that for component C2 the Fe abundance is relatively “sub-solar” and nearly constant ($\sim 0.2\text{--}0.4 Z_{\text{Fe},\odot}$), while the Si abundance is observed at near solar values ($0.5\text{--}1.0 Z_{\text{Si},\odot}$) at day ~ 1700 , with mild ($\sim 2\times$) variation through day ~ 6500 , before rising to values of $3\text{--}4 Z_{\text{Si},\odot}$. The Mg and S abundances for component C2 increase with time, similar to Si (see Table 4.1).

In Figure 4.5, we compare the abundances obtained for model M5 at epoch 2009, relative to Si, with the CSM and ejecta abundances from the simulations of D10. In D10, the CSM abundances were constrained by epoch 2000, while the ejecta abundances by epoch 2009. Hence, it is most relevant to compare the C1 and C2 abundances with the ejecta values from D10. In general, we find that aside from Fe in component C1, the abundances of both C1 and C2 are in reasonable agreement with D10. The higher Fe abundances found in our work arise from our more precise fitting of the velocity profile, and in particular the assumption that strong absorption affects the redshifted portion of the emission line (hence increasing the intrinsic Fe abundance required).

Increasing the timespan probed from ~ 3500 to ~ 7000 days helps considerably to constrain abundance variation trends. The strong differences in the abundances of components C1 and C2 (see Table 4.1), as well as the high and increasing values, naively imply strong a constant density over the emission region. The ejecta profile in particular is expected to have strong exponential radial dependence at early times, which could bias the flux, velocity, temperature, column densities and abundances estimates.

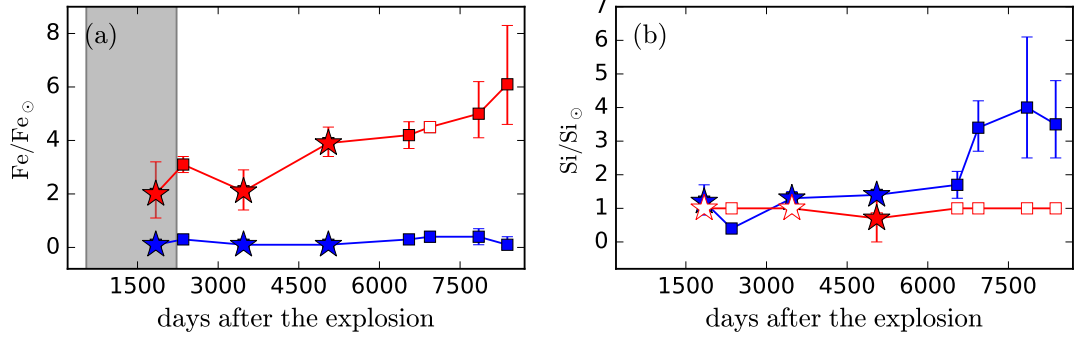


Figure 4.4: Same as Fig. 4.1 but panels (a) and (b) show the Fe and Si abundances, respectively.

Table 4.1: Best-fit abundance distributions as deduced from model M5. *Col. 1:* Epoch of combined X-ray observations. *Col. 2:* Components of model M5. *Col. 3-9:* Abundances of select elements with $Z \geq 10$ in solar units ($Z_{x,\odot}$).

Epoch	Component	Ne	Mg	Si	S	Ar	Ca	Fe
2000	C_1	1.0(fix)	1.0(fix)	1.0(fix)	1.0(fix)	$17.5^{+14.6}_{-11.0}$	1.0(fix)	$2.0^{+1.2}_{-0.9}$
	C_2	1.0(fix)	$0.4^{+0.5}_{-0.4}$	$1.2^{+0.5}_{-0.4}$	$2.9^{+1.3}_{-1.1}$	1.0(fix)	1.0(fix)	$0.1^{+0.1}_{-0.1}$
2001	C_1	1.0(fix)	1.0(fix)	1.0(fix)	$6.4^{+1.6}_{-1.5}$	$2.6^{+4.0}_{-2.6}$	1.0(fix)	$3.1^{+0.3}_{-0.3}$
	C_2	$0.6^{+0.2}_{-0.2}$	$0.4^{+0.1}_{-0.1}$	$0.4^{+0.1}_{-0.1}$	$0.1^{+0.1}_{-0.1}$	1.0(fix)	1.0(fix)	$0.3^{+0.1}_{-0.1}$
2004	C_1	1.0(fix)	1.0(fix)	1.0(fix)	$1.7^{+3.8}_{-1.7}$	$7.3^{+7.3}_{-6.2}$	1.0(fix)	$2.9^{+0.8}_{-0.7}$
	C_2	$0.2^{+0.3}_{-0.2}$	$0.8^{+0.3}_{-0.2}$	$1.3^{+0.2}_{-0.2}$	$1.9^{+0.6}_{-0.6}$	$1.0^{+1.0}_{-1.0}$	1.0(fix)	$0.1^{+0.1}_{-0.1}$
2009	C_1	1.0(fix)	1.0(fix)	$0.7^{+0.8}_{-0.7}$	$0.7^{+1.3}_{-0.7}$	$1.2^{+2.6}_{1.2}$	$2.4^{+2.9}_{-2.4}$	$3.9^{+0.6}_{-0.5}$
	C_2	$0.3^{+0.1}_{-0.1}$	$0.7^{+0.1}_{-0.1}$	$1.4^{+0.1}_{-0.1}$	$1.5^{+0.2}_{-0.2}$	$1.7^{+0.6}_{-0.5}$	$0.2^{+0.7}_{-0.1}$	$0.1^{+0.1}_{-0.1}$
2013	C_1	1.0(fix)	1.0(fix)	1.0(fix)	$9.5^{+3.2}_{-3.0}$	$15.7^{+7.7}_{-7.1}$	1.0(fix)	$4.2^{+0.5}_{-0.5}$
	C_2	1.0(fix)	$1.0^{+0.6}_{-0.5}$	$1.7^{+0.4}_{-0.4}$	1.0(fix)	1.0(fix)	1.0(fix)	$0.3^{+0.1}_{-0.1}$
2014	C_1	1.0(fix)	1.0(fix)	1.0(fix)	1.0(fix)	1.0(fix)	1.0(fix)	4.5(fix)
	C_2	1.0(fix)	2.4(fix)	$3.4^{+0.8}_{-0.7}$	2.7(fix)	1.0(fix)	1.0(fix)	$0.4^{+0.2}_{-0.2}$
2016	C_1	1.0(fix)	1.0(fix)	1.0(fix)	$14.4^{+7.5}_{-6.5}$	1.0(fix)	1.0(fix)	$5.0^{+1.2}_{-0.9}$
	C_2	1.0(fix)	2.9(fix)	$4.0^{+2.1}_{-1.5}$	$3.7^{+2.5}_{-2.1}$	1.0(fix)	1.0(fix)	$0.4^{+0.3}_{-0.3}$
2018	C_1	1.0(fix)	1.0(fix)	1.0(fix)	9.5(fix)	15.7(fix)	1.0(fix)	$6.1^{+2.2}_{-1.5}$
	C_2	1.0(fix)	1.0(fix)	$3.5^{+1.3}_{-1.0}$	1.0(fix)	1.0(fix)	1.0(fix)	$0.1^{+0.3}_{-0.1}$

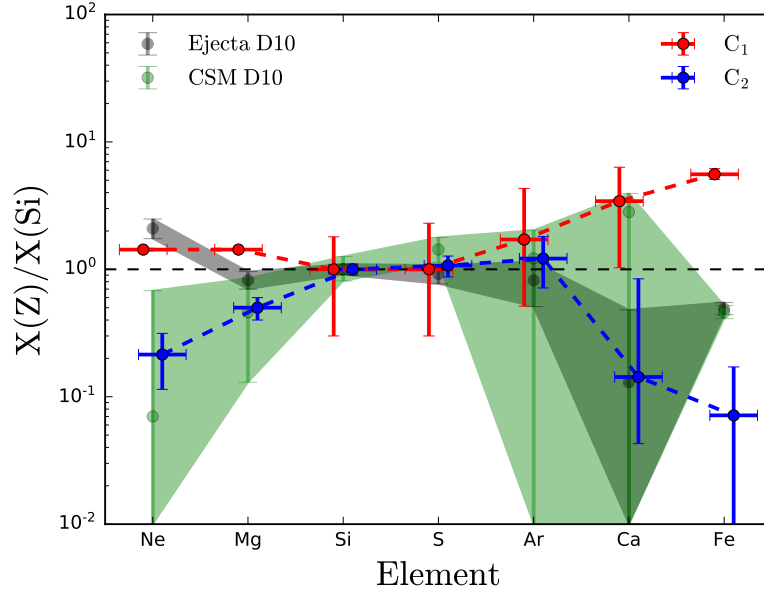


Figure 4.5: Relative abundances derived from components C1 and C2 of model M5 at epoch 2009, compared to the abundances of the CSM (*green* region) and ejecta (*grey* region) obtained in D10. The abundances are expressed relative to Si.

metal enhancement from shocked ejecta material, perhaps due to mixing of shocked ejecta and CSM via Rayleigh-Taylor instabilities. Importantly, the abundances of both components C1 and C2 rise with time. Based on the simulations of D10, the reverse/reflected shock should dominate the evolution after ~ 7 years (see panel (b) of Fig. 4.3) and naturally lead to an increase in abundances, in agreement with the data. The fact that the 1-D model explains the majority of the observed X-ray continuum and lines, and most of their variation in time, implies it cannot be too far off. One wrinkle, however, lies in the possible late-time rise of the Si abundance of component C2, which we have tentatively assigned with the forward shock. Are we seeing enhanced abundances from the shocked CSM? Or a possible contribution from a reverse shock? Unfortunately the error bars of the late-time data are quite large and there may be degeneracies due to fixed parameters.

In X-ray bright SNe such as 1987A and 2010jl, the observed X-ray emission is thought to arise predominantly from the shocked CSM (Michael et al. 2002; Katsuda et al. 2014,

2016) because the emission measure behind the blast wave is larger than behind the reverse shock; i.e. the region with the higher density should dominate the SN emission. Several authors consider two plasma components to fit the SNe X-ray spectra, where typically one component is associated with the forward shock emission region while the other is related to the reverse shock emission region (e.g., Yamaguchi et al. 2008, 2011; Frank et al. 2016; Schlegel et al. 2004; Chandra et al. 2009a; Nymark et al. 2009). Others argue that both components arise from the shocked CSM (Katsuda et al. 2016; Michael et al. 2002). More rarely, researchers consider additional non-thermal components to understand the role of synchrotron or inverse Compton processes (Tsubone et al. 2017). For SN 1996cr, we also find that two plasmas are necessary to explain the X-ray emission. Based on comparisons between the D10 model and the best-fitted velocities, column densities, abundances and fluxes beyond day ~ 2300 , we associate components C1 and C2 with the reverse (reflected) and forward shocked regions, respectively. The situation is less clear for the first two epochs, however, as the C1 and C2 components show the opposite trend compared to the D10 models, and we might be tempted to associate them with forward and reverse (reflected) shocked regions, respectively. This noticeable deviation may highlight possible asymmetries in the shocks or subtle modifications that are required in the assumed 1-D density profile.

Using the normalization parameter of model M5, we can estimate the effective electron density (n_e) of the shocked emission regions related to components C1 and C2. To obtain n_e , we assume that the X-ray emission region is a spherical cap defined by the best-fit opening angle and adopt typical radial thickness and profile values as a function of time from D10. The thickness and profile depend on whether the emission arises from C1 (shocked ejecta) or C2 (shocked CSM). Here we implicitly assume that these quantities do not deviate strongly from the estimates of D10 and furthermore that the electron density remains uniform in the angular direction (i.e., uniform density surface area at a given radius). For the 2000, 2004 and 2009 epochs, where we have HETG spectral resolution, the n_e estimates are $\sim 7.2, 2.9, 1.7 \times 10^5 \text{ cm}^{-3}$ for C1, respectively, and $\sim 1.9, 1.1, 0.8 \times 10^5 \text{ cm}^{-3}$ for C2,

respectively. This implies that between 2000 and 2009 the electron density decreases by a factor of ~ 4.2 and ~ 2.4 for both C1 and C2, respectively. Furthermore, these values are in rough agreement with the densities calculated by D10, and expected by Bauer et al. (2008) $n_e \geq 10^5 \text{ cm}^{-3}$.

Taking all of the above derived parameters into account, we argue that the most plausible scenario to explain the X-ray spectra of SN 1996cr at different epochs is as follows. After the explosion, an (a)spherical ejecta outflow emerges (if aspherical, it should have a $\approx 2\pi$ opening angle). The shockwave initially interacts with the sparse CSM inside the wind-blown shell, constrained only by a few weak X-ray upper limits. After a few years, the shockwave encounters the dense shell. The shell is likely asymmetric, perhaps oblate, or it may be that both the ejecta and the shell are asymmetric. In the case of symmetric ejecta, it would collide with the oblate shell at the poles first, and likely concentrate a strong, fast reflected shock back into a narrow angular region of the expanding ejecta. Alternatively, for asymmetric ejecta and an (a)spherical shell, we might also expect a concentrated, narrow-angle reflect shock. In both cases, the forward shock that eventually emerges would initially be highly collimated, but since there is nothing restricting it, it would rapidly fan out and become more spherical with time due to overpressure. Meanwhile, the reflected shock, which is strong and fast, would move further back into the ejecta; if the ejecta profile is still exponential, this might have the effect of weighting the dominant emission to small portions of the overall shock. For the symmetric ejecta and oblate shell scenario, the remainder of the ejecta should slowly collide with the more distant parts of the dense shell. Naively, we might expect the reflected shock opening angle to increase with time. However, the reflected shock may not be as strong in the outer portions of the shell (since the forward shock had to traverse a larger distance and perhaps was slower). Since it is colliding at an angle, it may end up pushing the reflected shock back in the direction of the initial reflected shock wave, or alternatively may just not be as efficient. Finally, the forward shock from the wider angle shell interaction will eventually emerge, further enforcing that the forward shock will become more spherically symmetric with time.

In summary, our observational results are well explained by considering a polar ejecta–CSM interaction, with M5 being the best-fitted model. We argue that the CSM is probably asymmetric, with an oblate shape, such that the observed shocks are strongly concentrate in polar directions. However, we cannot rule out an asymmetry in the ejecta. We find rough consistency with the previous simulations of D10, although clear discrepancies remain. Tables 3.2 and 4.1 show the parameters’ values obtained with our best-fit M5 at each epoch, which are plotted in Figures 4.1–4.4.

Chapter 5

Conclusions and future work

In this thesis, we analyzed eight epochs of *Chandra* HETG and *XMM-Newton* X-ray spectra for SN 1996cr, spanning ~ 1700 – 8900 days after the SN explosion. Thanks to the spectral resolution of the HETG, we resolve Hydrogen-like and Helium-like emission lines of Ne, Mg, Si, S, and Fe, permitting unprecedented high resolution X-ray spectroscopy. We developed a number of geometrical convolution models, which we applied to non-equilibrium ionization plasma models of the ejecta-CSM interaction, in order to match well the continuum and emission line profiles from the X-ray spectra. Based on this, we determined a best-fit geometrical ejecta-CSM shock structure that surrounds the SN explosion, with strong limits on spectral and geometrical parameters. Specifically:

- We develop a convolution model in XSPEC called `shellblur` to model partial sections of a symmetric expanding shell, including possible internal absorption by a uniform density medium. We use this model in conjunction with NEI `vpshock` models to simultaneously fit the emission line-profiles and continua of X-ray spectra for SN 1996cr.
- The X-ray spectra of SN 1996cr are well explained by a CSM–ejecta interaction model undergoing an obscured, symmetric ‘shell-like’ expansion. However, the observed emission line profiles require covering factors substantially less than 4π ;

i.e., shock regions which are distinctly not spherically symmetric. In particular, our best-fit model M5 requires at least two unique shellblur components (C1 and C2) with different NEI plasma temperatures, abundances and line-of-sight column densities. This polar geometrical interpretation is similar to that proposed by Dewey et al. (2011) with two components, one faster along the polar axis and another more spherically symmetric surrounding it.

- The preferred interaction geometry of the C1 and C2 components are well-defined polar cap structures, with a common inclination angle of $\approx 55^\circ$ and half-opening angles of $\approx 20 \pm 5^\circ$ and $\approx 58 \pm 4^\circ$, respectively. Both full solid angle and equatorial belt models fail to reproduce the variety of emission line shapes from our multi-epoch HETG spectra. We cannot, however, rule out a model comprised of numerous unresolved clumpy shocked regions, since this can arbitrarily fit all line fluxes and velocities.
- The hotter and more heavily obscured narrow polar component C1 is associated primarily with the Fe XXVI and Fe XXV emission lines and the >4 keV continuum. The best-fit temperature of this component is $\approx 9\text{--}30$ keV, with evidence for a mild decline with time. The line-of-sight column density is initially high ($\approx 2 \times 10^{22} \text{ cm}^{-2}$), but drops after day ~ 5000 , to potentially Galactic-only values. The cooler and less obscured wide polar component C2 is associated primarily with the Ne, Fe XXIV, Mg, S, and Si emission lines and the <4 keV continuum. The best-fit temperature of this component is $\approx 2\text{--}3$ keV, with evidence for a mild decline with time. The line-of-sight column density is generally low ($\approx 1\text{--}10 \times 10^{21} \text{ cm}^{-2}$) and potentially consistent with Galactic-only values.
- The strong difference between the early C1 and C2 line-of-sight column densities implies that either: (i) the components are evolving in regions with very different CSM densities which do not overlap strongly along the line-of-sight; (ii) the components are perhaps radially or angularly offset, such that the C1 emission is absorbed

by dense shocked material swept up in the C2 shock; *(iii)* the enhanced absorption arises from dense clumps in close proximity to or likely embedded within the C1 shock itself.

- Assuming the emission-line velocity profiles are intrinsically symmetric (i.e., geometrically reflected) but obscured by inner ejecta, we estimate the ejecta column density $N_{\text{ejecta}} = 6.0^{+1.4}_{-1.2} \times 10^{23} \text{ cm}^{-2}$ for C1, and $2.0^{+0.4}_{-0.3} \times 10^{22} \text{ cm}^{-2}$ for C2. Both values are much higher than the observed line-of-sight columns, reinforcing the idea that strong clumping of the ejecta and/or the CSM may be prevalent, perhaps in close proximity to or likely embedded within the shock structure. The difference by a factor of ~ 7 indicates that substantially denser and more inhomogeneous material is likely associated with the narrow-angle C1 shock region along the line-of-sight.
- The expansion velocities of both components are seen to increase to maxima of $\sim 6000 \text{ km s}^{-1}$ between days ~ 1700 – 3500 . This is roughly the epoch when the forward shock is thought to exit the dense-shell bubble in the D10 model. The expansion velocity is low at day ~ 1800 and increases slowly (considering uncertainties) until day ~ 3500 . The velocities then decrease substantially between days ~ 3500 – 5000 , but are poorly constrained thereafter and may remain constant. The lower velocities we find beyond ~ 5000 days compared to the D10 predictions may be a consequence of a somewhat higher CSM density. The evolution of the SN expansion velocity should be strongly correlated with the features of medium within which it moves, and hence should remain a valuable probe of the potentially clumpy and aspherical CSM density sculpted by the evolutionary phases prior to the SN (e.g., the evolution from MS to RSG to WR). Nevertheless, we cannot rule out the degree of asymmetry by the ejecta material, which affects the velocity of expansion.
- The total X-ray flux reaches a broad maximum between days ~ 3400 – 5000 (epochs 2004–2009), while individual components C1 and C2 reach maxima around days ~ 3400 and ~ 5000 , respectively. The more heavily obscured C1 component domi-

nates the total flux at all times. The flux in both components appears to be declining at late epochs, although not very smoothly, implying that the shocks may be encountering a progenitor CSM shaped by episodic RSG mass loss prior to the explosion. We note that the late-time fluxes of components C1 and C2 show reasonable agreement with the model shocked ejecta and CSM fluxes from D10, respectively, while at early times the assignment appears reversed.

- The asphericity of the ejecta-CSM interaction could arise from an inhomogeneous CSM, while the explosion itself was spherically symmetric (Dwarkadas 2007a; van Marle et al. 2012). Considering a spherical uniform distribution of mass for the ejecta, and using the C2 ejecta density, we estimate an average ejecta mass of $M_{\text{ejecta}} \sim 6.9 M_{\odot}$ at 2009. For 2004, we obtain a similar ejecta mass of $M_{\text{ejecta}} \sim 5.3 M_{\odot}$. These are in agreement with the model predictions from D10 of $M_{\text{ejecta}} = 4.5 M_{\odot}$.
- We find that component C1 exhibits a super-solar Fe abundance, while component C2 exhibits super-solar Ne, Mg, S, and Si abundances. The abundances generally increase with time, naively implying potential metal enhancement from shocked ejecta material, perhaps due to "fingers" from Rayleigh Taylor instabilities (in the case of the forward shocked component C2) or simply that the opacity to X-rays is diminishing with time, allowing us to see deeper into the ejecta material (in the case of component C1).
- The geometrical inclination and opening angles do not appear to evolve strongly with time, suggesting the two shock regions are well-formed, relatively static structures.
- It remains unclear whether the observed non-spherical structure arises from the CSM or ejecta. There is direct observational evidence for asymmetric CSM, such as in SN 1987A (Blondin & Lundqvist 1993; Michael et al. 2002) and evolved massive stars like η Carinae (Smith et al. 2007; Davidson & Humphreys 1997) or Betelgeuse (Kervella et al. 2018). Alternatively, there is some evidence of asymmetric ejecta,

such as in Cas A (Willingale et al. 2002; Grefenstette et al. 2014) and SN 1987A (Larsson et al. 2016).

- In the 2000 and 2001 epoch spectra, we observe an emission line excess at ~ 7.4 keV which is not fit with the M5 model. Interpreting this as an additional plasma with a jet-like structure implies an blueshifted expansion velocity of $\sim 23000 \text{ km s}^{-1}$ composed mainly of highly ionized Fe with $\sim 85 Z_{Fe, \odot}$. This component is not seen in later spectra.
- A plausible scenario to explain our data considers an (a)spherical ejecta interacting with an oblate dense shell and sparse outer CSM beyond. The ejecta collides with the dense shell at the poles first, sending a strong, fast reflected shock (C1) back into the ejecta over a narrow angle. The forward shock (C2) that eventually emerges is highly collimated at first but rapidly becomes more spherical with time due to overpressure. A wider angle shock travels outward and impacts the more distant portions of the shell at a slower pace; this leads to wide-angle forward and reflected shocks, although their overall efficiency and emissivity may be much weaker.
- Other interpretations may be possible, such as a combination of a more spherical reflected shock coupled with a more focused part. The current degeneracies likely imply that the interaction of the ejecta and CSM is complex.

Our results are in rough agreement with the simulation made by D10, which found that the SN 1996cr exploded in a low density medium before encountering a dense shell created by a previous interaction between a fast WR-wind and a slow RSG-wind from a preceding evolutionary stage of the progenitor. Additionally, our results are consistent with the 3-D analysis made by Dewey et al. (2011), whereby either the CSM of SN 1996cr must be non-uniform or the explosion/ejecta was highly asymmetric. The key difference is that we find two distinct components which are coupled to different temperatures, abundances and internal obscurations. Some parameter similarities from each component are seen with the D10 simulation parameters, with C2 perhaps sharing more overall similarities. The

expansion velocities we find compare well with the simulations at early epochs, but shift to lower values from day ~ 5000 , by up to a factor of 2 depending on which component we are comparing to; largely due to the fact that, at the time, D10 did not have observations to constrain the simulations. Future work will investigate a more realistic model that accounts for the two geometrical components, velocity profiles and abundance trends. Perhaps in the future, similar CSM/ejecta sleuthing will be possible for more SNe and even gamma-ray burst remnants, particularly once the ATHENA (Advanced Telescope for High ENergy Astrophysics) and XARM (X-ray Astronomy Recovery Mission) X-ray observatories fly (Barcons et al. 2017; Ishisaki et al. 2018).

There are several interesting trends seen in the 18 years of evolution observed thus far for SN 1996cr. However, several of these are only loosely constrained at present due to the relatively poor signal-to-noise and spectral resolution of the *XMM-Newton* data. A new deep *Chandra* HETG campaign to constrain the ejecta-CSM interaction geometry beyond day 10000 is needed to ultimately understand the fate of SN 1996cr at late times and constrain the CSM density of the purported outer RSG-wind. Since the shock in SN 1996cr appears to be at a latter stage, having now passed the dense shell, its evolution may provide important clues about what to expect for SN 1987A.

Bibliography

Anders E., Grevesse N., 1989, *Geochimica Cosmochimica Acta*, 53, 197

Arévalo P., et al., 2014, *ApJ*, 791, 81

Arnaud K. A., 2004, *ApJ*, p. submitted

Arnaud K., Smith R., Siemiginowska A., 2011, *Handbook of X-ray Astronomy*. Cambridge University Press

Barcons X., et al., 2017, *Astronomische Nachrichten*, 338, 153

Bartel N., Bietenholz M. F., 2008, *ApJ*, 682, 1065

Bartel N., Karimi B., Bietenholz M. F., 2017, *Astronomy Reports*, 61, 299

Bauer F. E., Brandt W. N., Sambruna R. M., Chartas G., Garmire G. P., Kaspi S., Netzer H., 2001, *AJ*, 122, 182

Bauer F. E., Dwarkadas V. V., Brandt W. N., Immler S., Smartt S., Bartel N., Bietenholz M. F., 2008, *ApJ*, 688, 1210

Bietenholz M., 2014, in *Proceedings of the 12th European VLBI Network Symposium and Users Meeting (EVN 2014)*. 7-10 October 2014. Cagliari, Italy. Online at <http://pos.sissa.it/cgi-bin/reader/conf.cgi?confid=230>, id.51. p. 51

Bietenholz M. F., Bartel N., Rupen M. P., 2010, *ApJ*, 712, 1057

- Bietenholz M. F., Brunthaler A., Soderberg A. M., Krauss M., Zauderer B., Bartel N., Chomiuk L., Rupen M. P., 2012, *ApJ*, 751, 125
- Bietenholz M. F., Kamble A., Margutti R., Milisavljevic D., Soderberg A., 2018, *MNRAS*, 475, 1756
- Bilinski C., et al., 2018, *MNRAS*, 475, 1104
- Blondin J. M., Lundqvist P., 1993, *ApJ*, 405, 337
- Borkowski K., Szymkowiak A. E., Blondin J. M.; Sarazin C. L., 1996, *ApJ*, 466, 866
- Borkowski K. J., Lyerly W. J., Reynolds S. P., 2001, *ApJ*, 548, 820
- Branch D., Wheeler J. C., 2017, *Supernova Explosions*. Springer, doi:10.1007/978-3-662-55054-0
- Canizares C. R., et al., 2005, *Publications of the Astronomical Society of the Pacific*, 117, 1144
- Cash W., 1979, *ApJ*, 228, 939
- Chandra P., 2018, *P. Space Sci Rev*, 214, 27
- Chandra P., et al., 2009a, *ApJ*, 690, 1839
- Chandra P., Dwarkadas V. V., Ray A., Immler S., Pooley D., 2009b, *ApJ*, 699, 388
- Chandra P., Chevalier R. A., Irwin C. M., Chugai N., Fransson C., Soderberg A. M., 2012a, *ApJ*, 750, L2
- Chandra P., Chevalier R. A., Chugai N., Fransson C., Irwin C. M., Soderberg A. M., Chakraborti S., Immler S., 2012b, *ApJ*, 755, 110
- Chandra P., Chevalier R. A., Chugai N., Fransson C., Soderberg A. M., 2015, *ApJ*, 810, 32
- Chevalier R. A., 1982a, *ApJ*, 259, 302

- Chevalier R. A., 1982b, *ApJ*, 259, L85
- Chevalier R. A., Blondin J. M., Emmering R. T., 1992, *ApJ*, 392, 118
- Crowther P. A., 2007, *ARA&A*, 45, 177
- Davidson K., Humphreys R. M., 1997, *ARA&A*, 35, 1
- DeLaney T., et al., 2010, *ApJ*, 725, 2038
- Dewey D., Noble M. S., 2009, in Bohlender D. A., Durand D., Dowler P., eds, *Astronomical Society of the Pacific Conference Series Vol. 411, Astronomical Data Analysis Software and Systems XVIII*. p. 234 ([arXiv:0902.1740](https://arxiv.org/abs/0902.1740))
- Dewey D., Zhekov S. A., McCray R., Canizares C. R., 2008, *ApJ*, 676, L131
- Dewey D., Bauer F. E., Dwarkadas V. V., 2011, in McEney J. E., Racusin J. L., Gehrels N., eds, *American Institute of Physics Conference Series Vol. 1358, American Institute of Physics Conference Series*. pp 289–292 ([arXiv:1102.1442](https://arxiv.org/abs/1102.1442)), doi:10.1063/1.3621791
- Dewey D., Dwarkadas V. V., Haberl F., Sturm R., Canizares C. R., 2012, *ApJ*, 752, 103
- Dickey J. M., Lockman F. J., 1990, *Ann. Rev. Astron. Astrophys.*, 28, 215
- Dwarkadas V. V., 2005, *ApJ*, 630, 892
- Dwarkadas V. V., 2007a, in *Revista Mexicana de Astronomia y Astrofisica Conference Series*. pp 49–56
- Dwarkadas V. V., 2007b, *ApJ*, 667, 226
- Dwarkadas V. V., 2008, *Physica Scripta*, 2008, 014024
- Dwarkadas V., Rosenberg D., 2013, *High Energy Density Physics*, 9, 226
- Dwarkadas V. V., Dewey D., Bauer F., 2010, *MNRAS*, 407, 812

- Dwarkadas V. V., Romero-Cañizales C., Reddy R., Bauer F. E., 2016, *MNRAS*, 462, 1101
- Eldridge J. J., Fraser M., Smartt S. J., Maund J. R., Crockett R. M., 2013, *Monthly Notices of the Royal Astronomical Society*, 436, 774
- Filippenko A. V., 1997, *ARA&A*, 35, 309
- Folatelli G., et al., 2014, *The Astrophysical Journal Letters*, 793, L22
- Foley R. J., Smith N., Ganeshalingam M., Li W., Chornock R., Filippenko A. V., 2007, *ApJ*, 657, L105
- Frank K. A., Zhekov S. A., Park S., McCray R., Dwek E., Burrows D. N., 2016, *ApJ*, 829, 40
- Freyer T., Hensler G., Yorke H. W., 2006, *ApJ*, 638, 262
- Garcia-Segura G., Mac Low M.-M., Langer N., 1996, *A&A*, 305, 229
- Garmire G. P., Bautz M. W., Ford P. G., Nousek J. A., Ricker G. R., 2003, *Proc.SPIE*, 4851
- Grefenstette B. W., et al., 2014, *Nature*, 506, 339
- Hoffman J. L., Leonard D. C., Chornock R., Filippenko A. V., Barth A. J., Matheson T., 2008, *ApJ*, 688, 1186
- Immler S., et al., 2005, *The Astrophysical Journal*, 632, 283
- Ishisaki Y., et al., 2018, *jltp*,
- Jansen F., et al., 2001, *A&A*, 365, L1
- Jerkstrand A., 2017, *Spectra of Supernovae in the Nebular Phase*. Springer International Publishing, pp 795–842, doi:10.1007/978-3-319-21846-5_29, https://doi.org/10.1007/978-3-319-21846-5_29

- Kaastra J. S., Paerels F. B. S., Durret F., Schindler S., Richter P., 2008, *Space Sci. Rev.*, 134, 155
- Katsuda S., Maeda K., Nozawa T., Pooley D., Immler S., 2014, *ApJ*, 780, 184
- Katsuda S., et al., 2016, *ApJ*, 832, 194
- Kervella P., et al., 2018, *A&A*, 609, A67
- Kimani N., et al., 2016, *A&A*, 593, A18
- Larsson J., et al., 2016, *ApJ*, 833, 147
- Leonard D. C., Filippenko A. V., Barth A. J., Matheson T., 2000, *ApJ*, 536, 239
- Levenson N. A., et al., 1997, *The Astrophysical Journal*, 484, 304
- Madsen K. K., Beardmore A. P., Forster K., Guainazzi M., Marshall H. L., Miller E. D., Page K. L., Stuhlinger M., 2017, *AJ*, 153, 2
- Magkotsios G., Timmes F. X., Hungerford A. L., Fryer C. L., Young P. A., Wiescher M., 2010, *The Astrophysical Journal Supplement Series*, 191, 66
- Margutti R., et al., 2014, *ApJ*, 780, 21
- Margutti R., et al., 2017, *ApJ*, 835, 140
- Martí-Vidal I., Marcaide J. M., Alberdi A., Guirado J. C., Pérez-Torres M. A., Ros E., 2011, *A&A*, 526, A142
- Mauerhan J., et al., 2014, *MNRAS*, 442, 1166
- Maund J. R., Smartt S. J., Kudritzki R. P., Podsiadlowski P., Gilmore G. F., 2004, *Nature*, 427, 129
- McCray R., 1993, *ARA&A*, 31, 175

- Meunier C., et al., 2013, MNRAS, 431, 2453
- Michael E., et al., 2002, ApJ, 574, 166
- Michael E., et al., 2003, ApJ, 593, 809
- Milisavljevic D., Fesen R. A., 2013, ApJ, 772, 134
- Montes M. J., Weiler K. W., Van Dyk S. D., Panagia N., Lacey C. K., Sramek R. A., Park R., 2000, ApJ, 532, 1124
- Nevalainen J., David L., Guainazzi M., 2010, A&A, 523, A22
- Nymark T. K., Fransson C., Kozma C., 2006, A&A, 449, 171
- Nymark T. K., Chandra P., Fransson C., 2009, A&A, 494, 179
- Orlando S., Miceli M., Pumo M. L., Bocchino F., 2015, The Astrophysical Journal, 810, 168
- Orlando S., Miceli M., Pumo M. L., Bocchino F., 2016, The Astrophysical Journal, 822, 22
- Park S., Zhekov S. A., Burrows D. N., Garmire G. P., Racusin J. L., McCray R., 2006, ApJ, 646, 1001
- Patnaude D. J., Lee S., Slane P. O., Badenes C., Heger A., Ellison D. C., Nagataki S., 2015, ApJ, 803, 101
- Patnaude D. J., Lee S. H., Slane P. O., Badenes C., Nagataki S., Ellison D. C., Milisavljevic D., 2017, ApJ, 849, 109
- Pooley D., et al., 2002, ApJ, 572, 932
- Reilly E., Maund J. R., Baade D., Wheeler J. C., Höflich P., Spyromilio J., Patat F., Wang L., 2017, MNRAS, 470, 1491

- Ross M., Dwarkadas V. V., 2017, *AJ*, 153, 246
- Salas P., Bauer F. E., Stockdale C., Prieto J. L., 2013, *MNRAS*, 428, 1207
- Sambruna R. M., Brandt W. N., Chartas G., Netzer H., Kaspi S., Garmire G. P., Nousek J. A., Weaver K. A., 2001, *ApJ*, 546, L9
- Schlegel E. M., 1990, *MNRAS*, 244, 269
- Schlegel D. J., Finkbeiner D. P., Davis M., 1998, *ApJ*, 500, 525
- Schlegel E. M., Kong A., Kaaret P., DiStefano R., Murray S., 2004, *ApJ*, 603, 644
- Smith N., 2006, *The Astrophysical Journal*, 644, 1151
- Smith N., 2013, *Monthly Notices of the Royal Astronomical Society*, 429, 2366
- Smith N., 2016, arXiv, p. submitted
- Smith R. K., Brickhouse N. S., Liedahl D. A., Raymond J. C., 2001, *ApJ*, 556, L91
- Smith N., et al., 2007, *ApJ*, 666, 1116
- Smith N., et al., 2010, *AJ*, 139, 1451
- Smith N., Mauerhan J. C., Prieto J. L., 2014, *MNRAS*, 438, 1191
- Smith N., Ginsburg A., Bally J., 2018, *MNRAS*, 474, 4988
- Stockdale C. J., et al., 2009, *Central Bureau Electronic Telegrams*, 1714
- Strüder L., et al., 2001, *A&A*, 365, L18
- Sturm R., Haberl F., Aschenbach B., Hasinger G., 2010, *A&A*, 515, A5
- Sugerman B. E. K., Crotts A. P. S., Kunkel W. E., Heathcote S. R., Lawrence S. S., 2005, *ApJS*, 159, 60

- Temple R. F., Raychaudhury S., Stevens I. R., 2005, *MNRAS*, 362, 581
- Thöne C. C., et al., 2017, *A&A*, 599, A129
- Tsubone Y., Sawada M., Bamba A., Katsuda S., Vink J., 2017, *ApJ*, 835, 34
- Turner M. J., et al., 2001, *A&A*, 365, L27
- Vink J., Kaastra J., Bleeker J., 1997, *A&A*, 328, 628
- Weisskopf M. C., Brinkman B., Canizares C., Garmire G., Murray S., Van Speybroeck L. P., 2002, *PASP*, 114, 1
- Willingale R., Bleeker J. A. M., van der Heyden K. J., Kaastra J. S., Vink J., 2002, *A&A*, 381, 1039
- Wilms J., Allen A., McCray R., 2000, *ApJ*, 542, 914
- Woosley S. E., Heger A., Weaver T. A., 2002, *Reviews of Modern Physics*, 74, 1015
- Yamaguchi H., Koyama K., Nakajima H., Bamba A., Yamazaki R., Vink J., Kawachi A., 2008, *PASJ*, 60, S123
- Yamaguchi H., Koyama K., Uchida H., 2011, *PASJ*, 63, S837
- Yamaguchi H., et al., 2014, *ApJ*, 785, L27
- Yaqoob T., Murphy K. D., 2011, *MNRAS*, 412, 1765
- Zanardo G., Staveley-Smith L., Ng C.-Y., Gaensler B. M., Potter T. M., Manchester R. N., Tzioumis A. K., 2013, *ApJ*, 767, 98
- Zhekov S. A., McCray R., Borkowski K. J., Burrows D. N., Park S., 2006, *ApJ*, 645, 293
- Zhekov S. A., McCray R., Dewey D., Canizares C. R., Borkowski K. J., Burrows D. N., Park S., 2009, *ApJ*, 692, 1190

den Herder J. W., et al., 2001, *A&A*, 365, L7

van Marle A. J., Keppens R., 2012, *A&A*, 547, A3

van Marle A. J., Smith N., Owocki S. P., van Veelen B., 2010, *MNRAS*, 407, 2305

van Marle A. J., Meliani Z., Marcowith A., 2012, *A&A*, 541, L8

Appendix A

XMM-Newton Spectra

In Figures A.1–A.5, we show the *XMM-Newton* *pn*-camera spectra for the epochs 2001, 2004, 2013, 2014, 2016, and 2018 (*black data points*), the best-fit model M5 (*black solid curve*) and the hotter and cooler components (*blue* and *red* dashed lines, respectively).

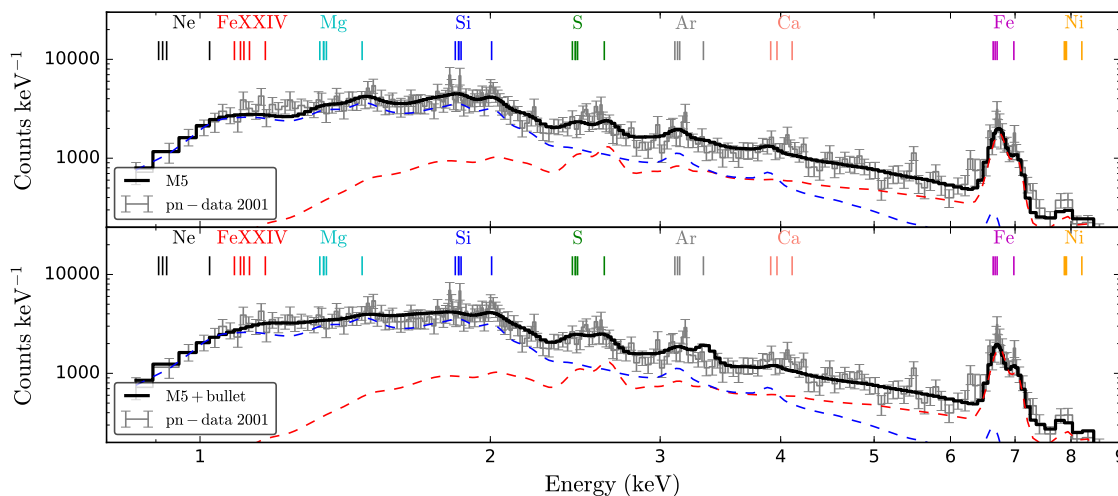


Figure A.1: (top) XMM-Newton pn-camera (black data points) X-ray spectrum and $1\text{-}\sigma$ errors from the 2001 epoch, as well as the best-fitting model M5 (with the black solid curve representing the total emission and the red and blue dashed curves indicating the hotter C1 and cooler C2 components, respectively). (bottom) same as the top panel, with the addition of a "bullet"-like third component; see §3.1.4. In both plots, vertical lines mark the rest-frame energies of well-known emission lines. The spectrum suffers from mild contamination at 6.4 keV due to poor subtraction of the emission from central AGN of the host galaxy.

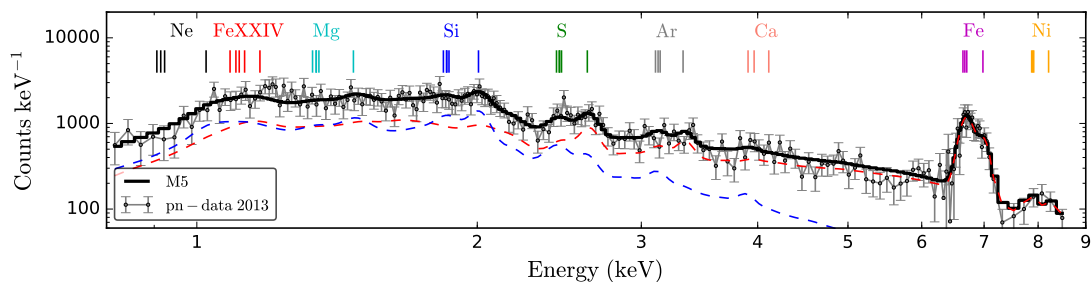


Figure A.2: Same as top panel of Fig. A.1 but for the 2013 epoch.

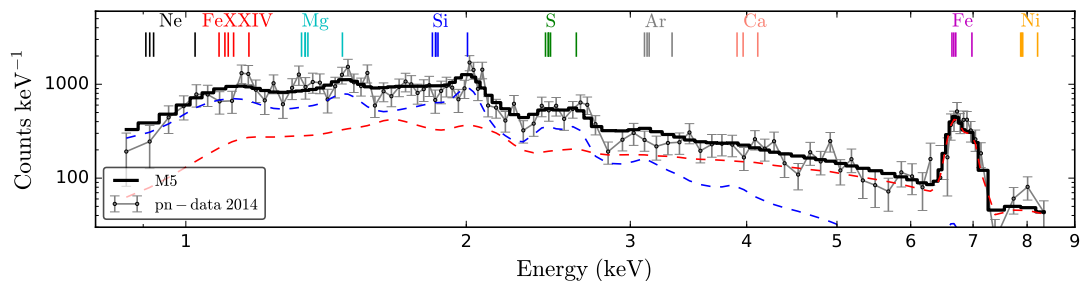


Figure A.3: Same as top panel of Fig. A.1 but for the 2014 epoch.

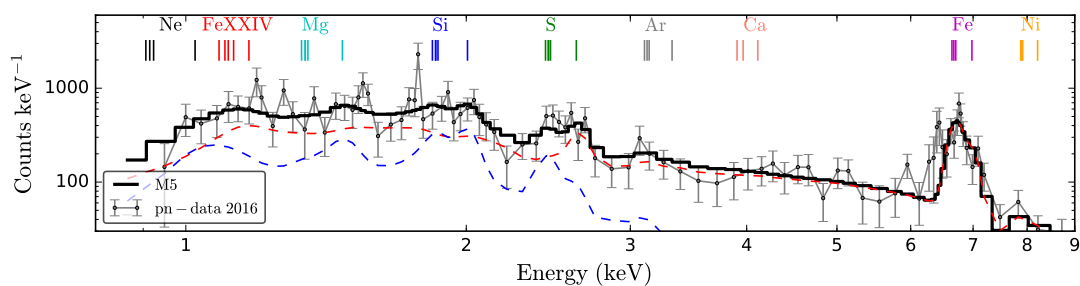


Figure A.4: Same as top panel of Fig. A.1 but for the 2016 epoch. The spectrum suffers from mild contamination at 6.4 keV due to poor subtraction of the emission from central AGN of the host galaxy.

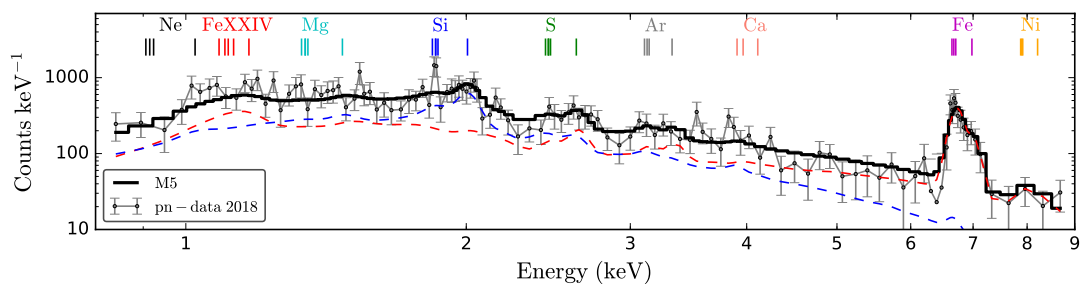


Figure A.5: Same as top panel of Fig. A.1 but for the 2018 epoch.